

RG-Invariant Symmetry Ratio for QCD: A Study of $U(1)_A$ and Chiral Symmetry Restoration

Ting-Wai Chiu,^{a,b,c,d,e,1} Tung-Han Hsieh^f

^a*Nuclear Science Division, Lawrence Berkeley National Laboratory, Berkeley, CA 94720*

^b*Department of Physics, National Taiwan University, Taipei, Taiwan 10617*

^c*Institute of Physics, Academia Sinica, Taipei, Taiwan 11529*

^d*Department of Physics, National Taiwan Normal University, Taipei, Taiwan 11677*

^e*Physics Division, National Center for Theoretical Sciences, Taipei, Taiwan 10617*

^f*Research Center for Applied Sciences, Academia Sinica, Taipei, Taiwan 11529*

E-mail: twchiu@phys.ntu.edu.tw, thhsieh@gate.sinica.edu.tw

ABSTRACT: We introduce a renormalization-group invariant observable, the symmetry strength parameter κ_{AB} , for the quantitative characterization of symmetry breaking in QCD. As a first application, we employ κ_{AB} to investigate the relative strength of $SU(2)_L \times SU(2)_R$ chiral symmetry and $U(1)_A$ axial symmetry breaking in $N_f = 2 + 1 + 1$ lattice QCD using optimal domain-wall fermions at the physical point. Our study covers three lattice spacings and twelve temperatures in the range 164–385 MeV. We examine three independent symmetry-breaking channels in the nonsinglet sector with connected correlators: the $U(1)_A$ -sensitive scalar–pseudoscalar channel (κ_{PS}), probing the π – δ system; the $SU(2)_L \times SU(2)_R$ -sensitive vector–axial–vector channel (κ_{VA}), probing the ρ – a_1 system; and an additional $U(1)_A$ -sensitive tensor–axial–tensor channel (κ_{TX}), probing the ρ_T – b_1 system. At finite lattice spacing, we observe a clear hierarchy $\kappa_{PS} > \kappa_{TX} \sim \kappa_{VA}$. A controlled continuum extrapolation reveals that this hierarchy collapses, with all three symmetry-breaking strengths becoming statistically indistinguishable within our precision. This result provides a new, model-independent benchmark from a chirally symmetric lattice action. Our findings indicate that the effective restoration scales for $SU(2)_L \times SU(2)_R$ and $U(1)_A$ in the nonsinglet sector converge closely near the chiral crossover, placing stringent quantitative constraints on the temperature window for chiral and axial symmetry manifestation in connected channels. These results support a two-stage restoration scenario, in which full symmetry restoration—including the singlet sector—occurs only at significantly higher temperatures once topological fluctuations are sufficiently suppressed.

¹Corresponding author.

Contents

1	Introduction	1
2	RG-invariant symmetry ratio	3
2.1	Correlation functions and symmetry partners	3
2.2	Renormalization and RG invariance	4
2.3	Integrated spectral weights and the symmetry strength parameter	5
2.4	Symmetry Channels Involving Flavor Singlet Operators	5
3	Lattice setup	9
4	Results	11
5	Continuum limit	14
6	Discussion and Outlook	17
6.1	Connections to topological susceptibility and singlet sector	18
6.2	Hierarchical restoration of chiral and axial symmetries	19
6.3	Broader symmetry landscape and emergent phases above T_c	21
6.4	Future computational improvements and extensions	22
6.4.1	Computational improvements and tensor singlet probes	22
6.4.2	Extension to flavor-singlet channels	23
6.5	RG interpretation and comparison with Pisarski–Wilczek analyses	23
6.6	Concluding remarks	26
A	Meson Operator Notation	27
B	Tables of results	28

1 Introduction

The pattern of symmetry realization is a defining feature of any quantum field theory, governing its phase structure and the spectrum of its excitations. In Quantum Chromodynamics (QCD), the theory of the strong interaction, two global symmetries play a pivotal role: the chiral $SU(2)_L \times SU(2)_R$ symmetry of the light (u, d) quark sector, and the $U(1)_A$ axial symmetry. In the vacuum, the former is spontaneously broken by the chiral condensate $\langle \bar{q}q \rangle$ [1, 2], giving mass to nucleons and generating pions as pseudo-Goldstone bosons. The latter is explicitly broken by the axial anomaly [3–5], contributing significantly to the mass of the η' meson [6–8]. A cornerstone of modern nuclear physics is understanding how

these broken symmetries behave under extreme conditions of temperature and density, such as those realized in heavy-ion collisions or within neutron stars.

The restoration of chiral symmetry is associated with the transition from a hadronic phase to a quark-gluon plasma (QGP). For QCD with physical quark masses, this is a smooth crossover occurring at a temperature $T_c \sim 156$ MeV [9–13].

A profound and long-standing question is whether the effective restoration of the $U(1)_A$ symmetry, linked to the suppression of topological gauge fluctuations, coincides with this chiral crossover or occurs at a distinctly higher temperature $T_1 > T_c$ [14–17]. Resolving this hierarchy is essential for a complete understanding of the QGP’s structure, the nature of the QCD transition, and the validity of effective models. Progress on this question via first-principles lattice QCD simulations has been challenging. A consistent picture among them has not emerged yet, see e.g., refs. [18–26], and the recent review by H.T. Ding at Lattice 2025¹, 2–8 November, Mumbai, India.

The $U(1)_A$ anomaly is particularly sensitive to lattice artifacts, and its clean study requires fermion discretizations that preserve chiral symmetry. Lattice studies with chiral fermions (domain-wall [27, 28] or overlap [29, 30]) have provided crucial insights [18, 19, 21, 24–26]. Notably, the JLQCD collaboration, using $N_f = 2$ Möbius domain-wall fermions with reweighting for overlap fermions at the lattice spacing 0.07 fm, found clear evidence that for $T > 190$ MeV, the $U(1)_A$ breaking is consistent with zero within statistical errors [24]. This is also consistent with studies using $N_f = 2 + 1 + 1$ optimal domain-wall fermions at the physical point and lattice spacing 0.063 fm, where $U(1)_A$ axial symmetry is restored for $T \gtrsim 190$ MeV [25]. However, refs. [24, 25] have not determined the $U(1)_A$ symmetry breaking for $T < 190$ MeV. On the other hand, in ref. [26], using $N_f = 2 + 1$ Möbius domain-wall fermions at multiple lattice spacings, the authors observed that the $U(1)_A$ axial symmetry is not restored for $T \lesssim 186$ MeV. To investigate whether any discrepancies between these different studies would occur for $T < 190$ MeV, a systematic approach to obtain definite continuum-extrapolated results for physical QCD with a chirally symmetric action remains a high-priority goal for the community. Addressing this goal requires overcoming two interconnected challenges: first, performing controlled continuum extrapolations across the temperature range of interest; second, developing a robust, quantitative observable to compare symmetry-breaking strength across different channels.

Traditional probes, such as hadron thermal and screening masses or the behavior of specific correlation functions at a single Euclidean space/time, can be ambiguous or sensitive to analysis choices. What is needed is a *renormalization-group (RG) invariant* measure that integrates spectral information, provides a clear normalization, and allows for a direct comparison between $SU(2)_L \times SU(2)_R$ and $U(1)_A$ breaking.

In this paper, we address both challenges. First, we introduce a novel, universal diagnostic: the *RG-invariant symmetry ratio* κ_{AB} . For two operators A and B related by a symmetry transformation, we define $\kappa_{AB} = (\chi_A - \chi_B)/(\chi_A + \chi_B)$, where $\chi_A \geq \chi_B > 0$ denote the corresponding susceptibilities derived from the regularized, vacuum-subtracted correlation functions. This construct is bounded $\kappa_{AB} \in [0, 1]$, and crucially RG-invariant

¹<https://indico.global/event/14504/contributions/137953/>

for exact symmetry partners, making it an ideal model-independent probe.

Second, we present the first application of κ_{AB} to the problem of symmetry restoration in QCD. We perform lattice simulations with $N_f = 2 + 1 + 1$ optimal domain-wall quarks at the physical point, using three lattice spacings and twelve temperatures in the range 164–385 MeV. We compute κ_{AB} across three distinct symmetry-breaking channels in the *nonsinglet* sector: the $U(1)_A$ -breaking (scalar, pseudoscalar) channel (κ_{PS}) probing the π - δ system; the $SU(2)_L \times SU(2)_R$ -breaking (vector, axial-vector) channel (κ_{VA}) probing the ρ - a_1 system; and an additional $U(1)_A$ -sensitive channel using tensor–axial-tensor operators (κ_{TX}) which probes the ρ_T - b_1 system through the $\bar{q}\gamma_4\gamma_k q$ and $\bar{q}\gamma_5\gamma_4\gamma_k q$ currents. The inclusion of the tensor channel provides a vital cross-check, as it probes the $U(1)_A$ anomaly through a different Dirac structure than the scalar channel.

Our key findings are as follows. At finite lattice spacing, we observe a clear ordering: the breaking in the $U(1)_A$ scalar–pseudoscalar channel is strongest, while the $U(1)_A$ tensor–axial-tensor channel and the $SU(2)_L \times SU(2)_R$ vector–axial-vector channel are significantly weaker and comparable to each other ($\kappa_{PS} > \kappa_{TX} \sim \kappa_{VA}$). However, a controlled continuum extrapolation reveals that this entire hierarchy collapses. All three symmetry-breaking strengths become statistically indistinguishable within our resolution. This result provides a new, high-precision benchmark from a chirally symmetric action. It indicates that the effective restoration scales probed by these different operators converge in the continuum limit, suggesting that the manifestations of $SU(2)_L \times SU(2)_R$ and $U(1)_A$ symmetries in the *nonsinglet* sector are much more concurrent than suggested by finite-lattice-spacing studies focused on a single channel.

The paper is organized as follows. In section 2, we formally define the RG-invariant symmetry ratio κ_{AB} and detail its theoretical properties. Our lattice setup, time-correlation functions, and analysis methodology are described in section 3. Numerical results at finite lattice spacing are presented in section 4, and the continuum extrapolation is performed in section 5. The implications of our findings and future applications of the κ_{AB} framework are discussed in section 6.

2 RG-invariant symmetry ratio

We introduce a renormalization-group invariant quantity that quantifies the degree of symmetry breaking in a quantum field theory. The construction relies on integrated spectral weights of Euclidean correlation functions for symmetry-related operators. Our measure, the *symmetry strength parameter* κ_{AB} , provides a global, scale-free indicator of symmetry violation and will be applied later to chiral symmetry restoration in finite-temperature QCD.

2.1 Correlation functions and symmetry partners

In a theory with an exact symmetry, correlation functions of operators related by the symmetry transformation must be degenerate. Consider the Euclidean time correlation function of a local meson operator

$$O_1^a(\vec{x}, t) = \bar{q}(\vec{x}, t) \Gamma t^a q(\vec{x}, t),$$

where Γ is a Dirac matrix specifying the quantum numbers of the channel, t^a (with $a = 1, \dots, N_f^2 - 1$) are the generators of $SU(N_f)$ for flavor nonsinglets, and $t^0 \equiv \mathbf{1} = \text{diag}(1, 1, \dots, 1)/\sqrt{2N_f}$ (identity operator) for the flavor singlet, with the normalization condition $\text{tr}(t^a t^b) = \delta^{ab}/2$ ($a = 0, \dots, N_f^2 - 1$). For flavor-singlet operators we adopt the shorthand notation $\bar{q}\Gamma q \equiv \bar{q}\Gamma t^0 q$, with the factor t^0 always implied but suppressed. We use the notation $(x_1, x_2, x_3, x_4) \equiv (x, y, z, t) \equiv (\vec{x}, t)$ interchangeably. With this notation, the t -correlator is defined as

$$C_\Gamma(t) = \int d^3x \langle O_\Gamma^a(\vec{x}, t) O_\Gamma^a(\mathbf{0}, 0) \rangle, \quad (2.1)$$

and its spatial counterpart, the z -correlator, as

$$C_\Gamma(z) = \int dx dy dt \langle O_\Gamma^a(x, y, z, t) O_\Gamma^a(\mathbf{0}, 0) \rangle. \quad (2.2)$$

If a symmetry is exact, the correlators of two partners A and B satisfy $C_A(t) = C_B(t)$ for any t and $C_A(z) = C_B(z)$ for any z .

Composite operators such as $O_\Gamma^a(x)$ require regularization and renormalization. Both $C_\Gamma(t)$ and $C_\Gamma(z)$ contain short-distance singularities; the leading divergence behaves as t^{-3} or z^{-3} in the continuum limit as the two operators approach coincidence, corresponding to a contact term $\sim a^{-3}$ on the lattice whose precise form is regularization-dependent. In what follows we concentrate on the t -correlator; the extension to the z -correlator is straightforward.

2.2 Renormalization and RG invariance

To quantify the deviation from degeneracy at a specific Euclidean time one may define a pointwise ratio

$$\kappa_{AB}(t) = \frac{C_A(t) - C_B(t)}{C_A(t) + C_B(t)}, \quad t \neq 0. \quad (2.3)$$

An analogous ratio $\kappa_{AB}(z)$ for spatial correlators has been employed to study $U(1)_A$ and $SU(2)_L \times SU(2)_R$ symmetry patterns in thermal QCD with optimal domain-wall fermions [31, 32].

For lattice formulations that preserve chiral symmetry (e.g., overlap or domain-wall fermions) the renormalization constants of symmetry-related operators are identical, $Z_A = Z_B$, because the transformation that relates O_A^a and O_B^a is a symmetry of the regularized lattice action. Concrete examples in two-flavor QCD include:

- under $U(1)_A$: the nonsinglet scalar (S , e.g. $\delta^+ \sim \bar{d}u$) and pseudoscalar (P , e.g. $\pi^+ \sim \bar{d}\gamma_5 u$) are partners, hence $Z_S = Z_P$;
- under $SU(2)_L \times SU(2)_R$: the nonsinglet vector (V , e.g. $\rho^+ \sim \bar{d}\gamma_i u$) and axial-vector (A , e.g. $a_1^+ \sim \bar{d}\gamma_5 \gamma_i u$) are partners, hence $Z_V = Z_A$;
- under $U(1)_A$ (tensor channel): the tensor (T , e.g. $\rho_T^+ \sim \bar{d}\gamma_4 \gamma_i u$) and axial-tensor (X , e.g. $b_1^+ \sim \bar{d}\gamma_5 \gamma_4 \gamma_i u$) are partners, hence $Z_T = Z_X$.

Consequently, the ratio $\kappa_{AB}(t)$ in eq. (2.3) is renormalization-group invariant, as the common factor $Z_A^2 = Z_B^2$ cancels between numerator and denominator.

2.3 Integrated spectral weights and the symmetry strength parameter

Although $\kappa_{AB}(t)$ is a valid probe, its dependence on t and the statistical fluctuations at individual times make a channel-wide comparison of symmetry breaking cumbersome. A more robust global measure is obtained by integrating over Euclidean time, which sums the spectral weight in each channel. We therefore define the *regularized susceptibility* for channel A . The contact term at $t = 0$ is subtracted to remove the short-distance singularity; for flavor-singlet and Cartan nonsinglet channels with scalar or tensor Dirac structure (for which the vacuum expectation value $\langle \bar{q}\Gamma_A t^a q \rangle$ is nonzero), the vacuum contribution is also subtracted. The integration runs over $t \in (0, 1/T)$, where T is the temperature, with the $t = 0$ contact term excluded:

$$\chi_A = \int_{0 < t < 1/T} dt \left[C_A(t) - \int d^3x \langle \bar{q}\Gamma_A t^a q \rangle_{\text{vev}}^2 \right], \quad (2.4)$$

where

$$\langle \bar{q}\Gamma_A t^a q \rangle_{\text{vev}} = \frac{1}{V} \int d^4x \langle \bar{q}(x)\Gamma_A t^a q(x) \rangle_{\text{F}}, \quad V = \int d^4x. \quad (2.5)$$

The subtraction of $C_A(0)$ and the vacuum term removes the dominant power divergence, leaving a multiplicatively renormalizable quantity: $\chi_A^R = Z_A^2 \chi_A$. An analogous definition holds for channel B .

Because $Z_A = Z_B$ for symmetry partners, we can now construct a global, RG-invariant measure of symmetry breaking, the *symmetry strength parameter*:

$$\boxed{\kappa_{AB} = \frac{\chi_A - \chi_B}{\chi_A + \chi_B}}, \quad (2.6)$$

where $\chi_A \geq \chi_B > 0$ (with the convention $\chi_A \geq \chi_B$ adopted without loss of generality), and $0 \leq \kappa_{AB} \leq 1$. This parameter provides an intuitive scale: $\kappa_{AB} = 0$ indicates exact degeneracy of the integrated spectral weights (the symmetry is manifest), whereas $\kappa_{AB} \rightarrow 1$ signals maximal asymmetry. The construction is general and can be applied to study any symmetry in quantum field theory for which partner operators can be defined.

Remark on terminology. Throughout this work, “restoration” of a symmetry always refers to *effective restoration* — i.e., the corresponding RG-invariant ratio κ_{AB} becomes consistent with zero within statistical uncertainties. Exact restoration, which would require vanishing quark masses for $SU(2)_L \times SU(2)_R$ and additionally the complete suppression of the $U(1)_A$ anomaly for $U(1)_A$ restoration, is neither achievable in physical QCD nor required for the validity of our conclusions. This operational definition is implicit in all subsequent uses of “degeneracy”, “restoration”, and “ $\kappa_{AB} = 0$ ”.

In the remainder of this paper we employ κ_{AB} to investigate the restoration patterns of the $U(1)_A$ and $SU(2)_L \times SU(2)_R$ symmetries in high-temperature lattice QCD.

2.4 Symmetry Channels Involving Flavor Singlet Operators

The full chiral $SU(2)_L \times SU(2)_R$ multiplet for $J = 0$ mesons includes not only the connected channels studied in this work, but also symmetry pairs involving flavor-singlet operators.

In principle, each pair could be probed by the symmetry ratio κ_{AB} defined in eq. (2.6), offering additional insight into chiral restoration.

For $N_f = 2$ massless QCD, effective restoration of $SU(2)_L \times SU(2)_R$ chiral symmetry implies equalities among regularized susceptibilities as shown in eqs. (2.7)–(2.11),

$$\chi_S^s = \chi_P^{ns} \iff \chi_\sigma = \chi_\pi, \quad (2.7)$$

$$\chi_P^s = \chi_S^{ns} \iff \chi_\eta = \chi_\delta, \quad (2.8)$$

$$\chi_{T_k}^s = \chi_{X_k}^{ns} \iff \chi_{\omega_T} = \chi_{b_1}, \quad k = 1, 2, 3, \quad (2.9)$$

$$\chi_{X_k}^s = \chi_{T_k}^{ns} \iff \chi_{h_{1T}} = \chi_{\rho_T}, \quad k = 1, 2, 3, \quad (2.10)$$

$$\chi_{V_k}^{ns} = \chi_{A_k}^s \iff \chi_\rho = \chi_{a_1}, \quad k = 1, 2, 3, \quad (2.11)$$

where the superscripts s and ns denote singlet and nonsinglet channels, respectively. Recall that the physical η' corresponds to the η singlet in $N_f = 2$ QCD. The notations of meson operators and their corresponding regularized susceptibilities are summarized in appendix A.

On the other hand, effective restoration of $U(1)_A$ axial symmetry implies eqs. (2.12)–(2.15).

$$\chi_S^{ns} = \chi_P^{ns} \iff \chi_\delta = \chi_\pi, \quad (2.12)$$

$$\chi_S^s = \chi_P^s \iff \chi_\sigma = \chi_\eta, \quad (2.13)$$

$$\chi_{T_k}^{ns} = \chi_{X_k}^{ns} \iff \chi_{\rho_T} = \chi_{b_1}, \quad k = 1, 2, 3. \quad (2.14)$$

$$\chi_{T_k}^s = \chi_{X_k}^s \iff \chi_{\omega_T} = \chi_{h_{1T}}, \quad k = 1, 2, 3, \quad (2.15)$$

Each equality corresponds to a distinct RG-invariant symmetry ratio κ_{AB} as defined in eq. (2.6).

Equality of renormalization constants from symmetry. For chirally symmetric fermion formulations, the symmetry relations in eqs. (2.7)–(2.15) imply specific equalities among renormalization constants.

For scalar and pseudoscalar channels, the partner relations yield:

- From $SU(2)_L \times SU(2)_R$: (σ, π) and (η, δ) are partners, giving $Z_S^s = Z_P^{ns}$ and $Z_P^s = Z_S^{ns}$.
- From $U(1)_A$: (δ, π) and (σ, η) are partners, giving $Z_S^{ns} = Z_P^{ns}$ and $Z_S^s = Z_P^s$.

Combining these gives:

$$Z_S^{ns} = Z_P^{ns} = Z_S^s = Z_P^s.$$

For tensor and axial-tensor channels, the same logic applies:

- Under $SU(2)_L \times SU(2)_R$: (T^s, X^{ns}) and (X^s, T^{ns}) are partners, giving $Z_T^s = Z_X^{ns}$ and $Z_X^s = Z_T^{ns}$.
- Under $U(1)_A$: (T^s, X^s) and (T^{ns}, X^{ns}) are partners, giving $Z_T^s = Z_X^s$ and $Z_T^{ns} = Z_X^{ns}$.

Combining these gives:

$$Z_T^{ns} = Z_X^{ns} = Z_T^s = Z_X^s.$$

For vector and axial-vector channels, the pattern is different:

- Under $SU(2)_L \times SU(2)_R$, the nonsinglet vector ρ and axial-vector a_1 are partners, giving $Z_V^{ns} = Z_A^{ns}$. Both currents are conserved for all m_q , so $Z_V^{ns} = Z_A^{ns} = 1$.
- The singlet vector $\omega \sim \bar{q}\gamma_\mu q$ is associated with the exact $U(1)_V$ symmetry of the QCD action, which is preserved for all m_q , so $Z_V^s = 1$.
- The singlet axial-vector $h_{1\mu} \sim \bar{q}\gamma_5\gamma_\mu q$ is *not conserved* due to the $U(1)_A$ anomaly, regardless of quark mass. Its divergence is $\partial^\mu h_{1\mu} = 2m_q\bar{q}\gamma_5 q + \frac{g^2}{16\pi^2}F\tilde{F}$. Unlike the conserved currents above, $h_{1\mu}$ is not protected by a conserved charge, so its renormalization constant Z_A^s is not fixed to unity and must be determined non-perturbatively. The current itself renormalizes multiplicatively (without operator mixing), but $Z_A^s \neq Z_V^s$ and $Z_A^s \neq 1$ in general.

These relations ensure that, after appropriate contact term and vacuum subtractions, *any* ratio κ_{AB} involving operators from the same renormalization constant multiplet is RG-invariant. This includes the nonsinglet ratios κ_{PS} , κ_{VA} , κ_{TX} studied in this work, as well as singlet-involved ratios such as $\kappa_{\sigma,\pi}$, $\kappa_{\eta,\delta}$, κ_{ω_T,b_1} , κ_{h_{1T},ρ_T} , and $\kappa_{\omega_T,h_{1T}}$. Consequently, ratios like $\kappa_{\sigma,\pi}$ and $\kappa_{\eta,\delta}$ are formally RG-invariant, just like their nonsinglet counterparts.

Despite this formal RG invariance, several practical obstacles prevent a clean extraction of κ_{AB} for channels involving flavor-singlet operators in the present study:

1. Disconnected diagrams and stochastic noise.

Correlators of the singlet operators σ and η' receive contributions from disconnected Wick contractions, which are computationally demanding and statistically noisy in lattice simulations and require extensive stochastic sampling. By contrast, their nonsinglet partners involve only connected diagrams. This asymmetry in diagrammatic structure leads to very different signal-to-noise ratios and systematic uncertainties in the estimation of the susceptibilities χ_A and χ_B , compromising a direct comparison.

2. Regularization of scalar and pseudoscalar singlet susceptibilities.

Following eq. (2.4), the regularized susceptibilities for singlet channels are defined by subtracting the power-divergent contact term. For the scalar singlet $\sigma \sim \bar{q}q$, this requires subtracting the vacuum expectation value $\langle \bar{q}q \rangle^2$ to remove the power divergence $\propto 1/a^2$. For the pseudoscalar singlet $\eta' \sim \bar{q}\gamma_5 q$, parity ensures $\langle \bar{q}\gamma_5 q \rangle = 0$ in the continuum, so no vacuum subtraction is needed. However, the *unsubtracted* bare susceptibility contains power-divergent mixing with the topological charge density $F\tilde{F}$ through coefficients $\sim 1/a^n$. The contact term subtraction in eq. (2.4) removes these power-divergent mixings as well. After this subtraction, the resulting regularized susceptibility $\chi_{\eta'}^{\text{sub}}$ is free of all power divergences and multiplicatively renormalizable with $Z_P^s = Z_S^{ns}$. *Crucially, all power-divergent mixings, including any power-divergent mixing with the topological susceptibility χ_t , are completely removed by these subtractions.*

3. Finite mixing with topological susceptibility.

Even after all power divergences are removed, the $U(1)_A$ anomaly induces finite physical mixing between the singlet susceptibilities and the topological susceptibility χ_t .

For the scalar singlet, this mixing occurs through a scale-independent coefficient:

$$\chi_\sigma^R = Z_S^2 \chi_\sigma^{\text{sub}} + c_S \chi_t^R,$$

where c_S is a finite, scheme-dependent constant; its scale independence follows from the fact that χ_σ and χ_t share the same CP quantum numbers and their mixing is mediated by a dimension-four operator whose anomalous dimension vanishes at leading order. For the pseudoscalar singlet, the mixing is through a scale-dependent coefficient:

$$\chi_{\eta'}^R = Z_S^2 \chi_{\eta'}^{\text{sub}} + \tilde{c}(\mu) \chi_t^R,$$

with $\tilde{c}(\mu)$ evolving under the renormalization group due to the interplay with the axial anomaly Ward identity. These mixing coefficients are **finite** — they are not power-divergent and cannot be removed by the subtractions of eq. (2.4). Obtaining the fully renormalized susceptibilities χ_σ^R and $\chi_{\eta'}^R$ therefore requires a non-perturbative determination of c_S and $\tilde{c}(\mu)$ [33].

Constructing fully RG-invariant ratios such as $\kappa_{\sigma,\pi}$ and $\kappa_{\eta,\delta}$ would then require performing a non-perturbative subtraction of the finite mixing terms. We defer this substantial task to future work.

For overlap fermions with exact chiral symmetry, the topological charge can be defined via the index theorem ($Q_t = n_+ - n_-$) through zero mode counting. In this case, χ_t requires no renormalization and the bare susceptibility equals the renormalized one: $\chi_t^{\text{bare}} = \chi_t^R$. This simplifies the analysis, but the challenge of determining the finite mixing coefficients remains. In practice, at finite lattice spacing, gauge field dislocations can produce spurious near-zero modes that contaminate the zero-mode count; sufficiently smooth configurations are required for the index theorem identification to be unambiguous.

4. Tensor singlet channels: a cleaner probe.

In contrast to the scalar and pseudoscalar singlets, the tensor singlet operators $\omega_{T,k} \equiv T_k^s = \bar{q}\gamma_4\gamma_k q$ and $h_{1T,k} \equiv X_k^s = \bar{q}\gamma_5\gamma_4\gamma_k q$ avoid both power-divergent mixings and finite mixing with χ_t . Their renormalization is purely multiplicative with $Z_T^s = Z_X^s$ in chirally symmetric formulations, making the ratio $\kappa_{\omega_T, h_{1T}} = (\chi_{\omega_T} - \chi_{h_{1T}})/(\chi_{\omega_T} + \chi_{h_{1T}})$ RG-invariant and theoretically clean. Mixed ratios $\kappa(\chi_{\omega_T}, \chi_{b_1})$ and $\kappa(\chi_{h_{1T}}, \chi_{\rho_T})$ similarly probe $SU(2)_L \times SU(2)_R$ restoration between singlet and nonsinglet tensor partners. Future studies with improved techniques for disconnected diagrams may enable reliable investigation of these channels.

Given these considerations, the present study focuses initially on the connected, non-singlet channels where the RG-invariant ratio κ_{AB} rests on the firmest theoretical and numerical ground:

- κ_{PS} (δ - π) for $U(1)_A$,
- κ_{VA} (ρ - a_1) for $SU(2)_L \times SU(2)_R$,

- κ_{TX} ($\rho_T b_1$) for $U(1)_A$ through a different Dirac structure.

These choices provide a clean, theoretically unambiguous, and statistically precise set of observables. The consistent picture emerging from these three channels (presented in section 4 and section 5) gives strong evidence for the relative restoration scales of $U(1)_A$ and $SU(2)_L \times SU(2)_R$ symmetries.

3 Lattice setup

We generate gauge ensembles using hybrid Monte Carlo (HMC) simulations of lattice QCD with $N_f = 2 + 1 + 1$ optimal domain-wall quarks [34, 35] at the physical point. The simulations are performed on $32^3 \times (16, 12, 10, 8)$ lattices with the plaquette gauge action [36] at three values of $\beta = 6/g^2 = (6.15, 6.18, 6.20)$, corresponding to lattice spacings $a \simeq (0.075, 0.069, 0.064)$ fm. These ensembles are produced with the same actions [37, 38] and algorithms as their counterparts on larger $64^3 \times (20, 16, 12, 10, 8, 6)$ lattices [39], but at one-eighth of the spatial volume. Simulations are carried out on GPU clusters equipped with various NVIDIA GPUs.

After initial thermalization, gauge configurations are sampled and distributed among 16–32 independent simulation units, each performing a separate HMC stream. In each stream, one configuration is sampled every five trajectories. All sampled configurations from all streams are combined to obtain the final ensemble. Lattice parameters and statistics for the meson t -correlator calculations are listed in table 1. The temperatures covered range from ~ 164 to 385 MeV, all above the pseudocritical temperature $T_c \sim 150$ MeV.

Lattice spacings and quark masses (u/d , s , c) are determined on $32^3 \times 64$ lattices with $\{460, 636, 726\}$ configurations for $\beta = \{6.15, 6.18, 6.20\}$, respectively. The lattice spacing is fixed using the Wilson flow [40, 41] with the condition $\{t^2 \langle E(t) \rangle\}|_{t=t_0} = 0.3$ and input $\sqrt{t_0} = 0.1416(8)$ fm [42]. The resulting spacings are listed in table 2. Physical quark

β	$a[\text{fm}]$	N_x	N_t	$T[\text{MeV}]$	N_{confs}	$(m_{u/d}a)_{\text{res}}$	$(m_s a)_{\text{res}}$	$(m_c a)_{\text{res}}$
6.15	0.075	32	16	164	359	$6.2(5) \times 10^{-5}$	$3.1(4) \times 10^{-5}$	$1.1(7) \times 10^{-5}$
6.18	0.069	32	16	179	324	$4.9(7) \times 10^{-5}$	$5.8(1.7) \times 10^{-5}$	$2.7(9) \times 10^{-5}$
6.20	0.064	32	16	192	588	$3.5(4) \times 10^{-5}$	$2.3(2) \times 10^{-5}$	$6.5(1.1) \times 10^{-6}$
6.15	0.075	32	12	219	409	$9.0(1.4) \times 10^{-5}$	$6.0(8) \times 10^{-5}$	$1.5(3) \times 10^{-6}$
6.18	0.069	32	12	238	781	$1.9(2) \times 10^{-5}$	$1.6(1) \times 10^{-5}$	$3.8(5) \times 10^{-6}$
6.20	0.064	32	12	257	514	$1.8(6) \times 10^{-5}$	$1.6(6) \times 10^{-5}$	$9.4(4.2) \times 10^{-6}$
6.15	0.075	32	10	263	496	$2.4(4) \times 10^{-5}$	$2.0(3) \times 10^{-5}$	$7.5(2.6) \times 10^{-6}$
6.18	0.069	32	10	286	377	$2.4(8) \times 10^{-5}$	$2.2(7) \times 10^{-5}$	$9.7(3.9) \times 10^{-6}$
6.20	0.064	32	10	308	481	$5.8(1.5) \times 10^{-6}$	$5.1(1.2) \times 10^{-6}$	$1.4(2) \times 10^{-6}$
6.15	0.075	32	8	328	640	$3.5(8) \times 10^{-5}$	$2.9(6) \times 10^{-5}$	$1.2(3) \times 10^{-5}$
6.18	0.069	32	8	357	302	$1.3(7) \times 10^{-5}$	$1.2(6) \times 10^{-5}$	$4.9(2.2) \times 10^{-6}$
6.20	0.064	32	8	385	468	$6.3(1.9) \times 10^{-6}$	$6.0(1.8) \times 10^{-6}$	$3.0(9) \times 10^{-6}$

Table 1: Lattice parameters and statistics of the twelve gauge ensembles used in this work. The last three columns give the residual masses of u/d , s , and c quarks [43].

β	$a[\text{fm}]$	$m_{u/d}a$	$m_s a$	$m_c a$
6.15	0.0751(5)	0.00200	0.064	0.705
6.18	0.0690(5)	0.00180	0.058	0.626
6.20	0.0641(4)	0.00125	0.040	0.550

Table 2: Lattice spacings and bare quark masses for $N_f = 2 + 1 + 1$ lattice QCD with optimal domain-wall quarks at the physical point.

masses are obtained by tuning the bare masses so that the lowest-lying states extracted from time-correlation functions of the meson operators $\{\bar{u}\gamma_5 d, \bar{s}\gamma_5 s, \bar{c}\gamma_5 c\}$ agree with the physical masses of $\pi^\pm(140)$, $\phi(1020)$, and $J/\psi(3097)$. The tuned bare quark masses are also given in table 2.

Chiral symmetry breaking due to the finite extent $N_s = 16$ in the fifth dimension is quantified by the residual masses of each quark flavor [43], listed in the last three columns of table 1. These residual masses are less than (4.5%, 0.1%, 0.005%) of the corresponding bare masses for ($u/d, s, c$) quarks, translating to less than (0.2, 0.1, 0.06) MeV/ c^2 , respectively. This confirms that chiral symmetry is well preserved and that the effective 4D Dirac operator for optimal domain-wall fermions remains accurate for both light and heavy quarks. Consequently, hadronic observables (such as meson correlators) can be computed with high precision, with uncertainties dominated by statistics and other systematics.

We now summarize the notations and conventions used in this work.

The correlation function of off-diagonal flavor-nonsinglet meson interpolator $\bar{q}_1 \Gamma q_2$ (e.g., $\bar{u}\Gamma d$) on a lattice with (N_x, N_y, N_z, N_t) sites is computed as

$$C_\Gamma(x) = \langle (\bar{q}_1 \Gamma q_2)_x (\bar{q}_1 \Gamma q_2)_0^\dagger \rangle = \left\langle \text{tr} [\Gamma (D_c + m_1)_{0,x}^{-1} \Gamma (D_c + m_2)_{x,0}^{-1}] \right\rangle_{\text{confs}}, \quad (3.1)$$

where $(D_c + m_q)^{-1}$ denotes the valence quark propagator with mass m_q in lattice QCD with exact chiral symmetry [44], tr is the trace over color and Dirac indices, and $\langle \dots \rangle_{\text{confs}}$ denotes the average over gauge configurations. Here $x = (x_1, x_2, x_3, x_4) = (x, y, z, t)$; an overall sign arising from $\gamma_4 \Gamma^\dagger \gamma_4 = \pm \Gamma$ has been suppressed. The temporal correlator is defined as

$$C_\Gamma(t, T) = \sum_{x_1, x_2, x_3} C_\Gamma(x), \quad (3.2)$$

where $T = 1/(N_t a)$ is the temperature. The regularized susceptibility (2.4) can be written as

$$\chi_\Gamma(T) = \sum_{t=1}^{N_t-1} C_\Gamma(t, T). \quad (3.3)$$

In this study we focus on the off-diagonal flavor-nonsinglet operator $\bar{u}\Gamma d/\sqrt{2}$, with

$$\Gamma = \{\mathbf{1}, \gamma_5, \gamma_k, \gamma_5 \gamma_k, \gamma_4 \gamma_k, \gamma_5 \gamma_4 \gamma_k, k = 1, 2, 3\},$$

corresponding to the scalar (S), pseudoscalar (P), vector (V), axial-vector (A), tensor-vector (T), and axial-tensor-vector (X) channels, respectively.

Thanks to S_3 symmetry, the correlators satisfy $C_{V_1} = C_{V_2} = C_{V_3}$, $C_{A_1} = C_{A_2} = C_{A_3}$, $C_{T_1} = C_{T_2} = C_{T_3}$, and $C_{X_1} = C_{X_2} = C_{X_3}$. To improve statistics, we average over the three spatial components for each channel, e.g.,

$$C_V(t, T) = \frac{1}{3} \sum_{k=1}^3 C_{V_k}(t, T),$$

and similarly for A , T and X .

These averaged correlators $C_\Gamma(t, T)$ are used to compute the regularized susceptibility of off-diagonal flavor nonsinglet mesons,

$$\chi_\Gamma(T) = \sum_{t=1}^{N_t-1} C_\Gamma(t, T)$$

and the RG-invariant symmetry ratios κ_{AB} defined in (2.6) for the channel pairs VA , PS , and TX . Here κ_{VA} probes $SU(2)_L \times SU(2)_R$ chiral symmetry restoration, while κ_{PS} and κ_{TX} probe $U(1)_A$ axial symmetry restoration.

4 Results

We begin by analyzing the temporal correlators $C_\Gamma(t)$ of the $\bar{u}\Gamma d$ bilinears at the three lowest temperatures, $T = (164, 179, 193)$ MeV, displayed in figure 1. Our focus is on the degeneracy patterns among the (V, A) , (P, S) , and (T, X) channels, which respectively reflect the restoration of $SU(2)_L \times SU(2)_R$ chiral symmetry and $U(1)_A$ axial symmetry.

As shown in figure 1, the correlators follow the ordering

$$C_P(t) \gtrsim C_S(t) > C_V(t) \gtrsim C_A(t) > C_T(t) \gtrsim C_X(t)$$

at all temperatures. This hierarchy corresponds to the ordering of meson thermal masses,

$$m_P \lesssim m_S < m_V \lesssim m_A < m_T \lesssim m_X,$$

which remains consistent across the full temperature range studied (164–385 MeV).

Within the resolution of our data, no splitting is observed inside the (P, S) , (V, A) , or (T, X) doublets, except for a mild deviation in the (P, S) channel at $T = 164$ MeV on the coarsest lattice ($a = 0.075$ fm), shown in the upper panel of figure 1. Since degeneracy in the (P, S) and (T, X) channels signals $U(1)_A$ restoration, the observed discrepancy is likely a lattice artifact due to finite lattice spacing.

To cleanly address this issue in the continuum limit, a renormalization-group (RG) invariant measure of degeneracy is required—one that can be extrapolated to $a \rightarrow 0$ and allows quantitative comparison of symmetry breaking across different channels. Standard probes, such as thermal hadron masses or single-time correlator values, can be ambiguous or sensitive to analysis details. Instead, we employ the RG-invariant symmetry ratio κ_{AB} defined in Eq. (2.6), which integrates spectral information, provides clear normalization, and enables direct comparison between $SU(2)_L \times SU(2)_R$ and $U(1)_A$ breaking in all channels.

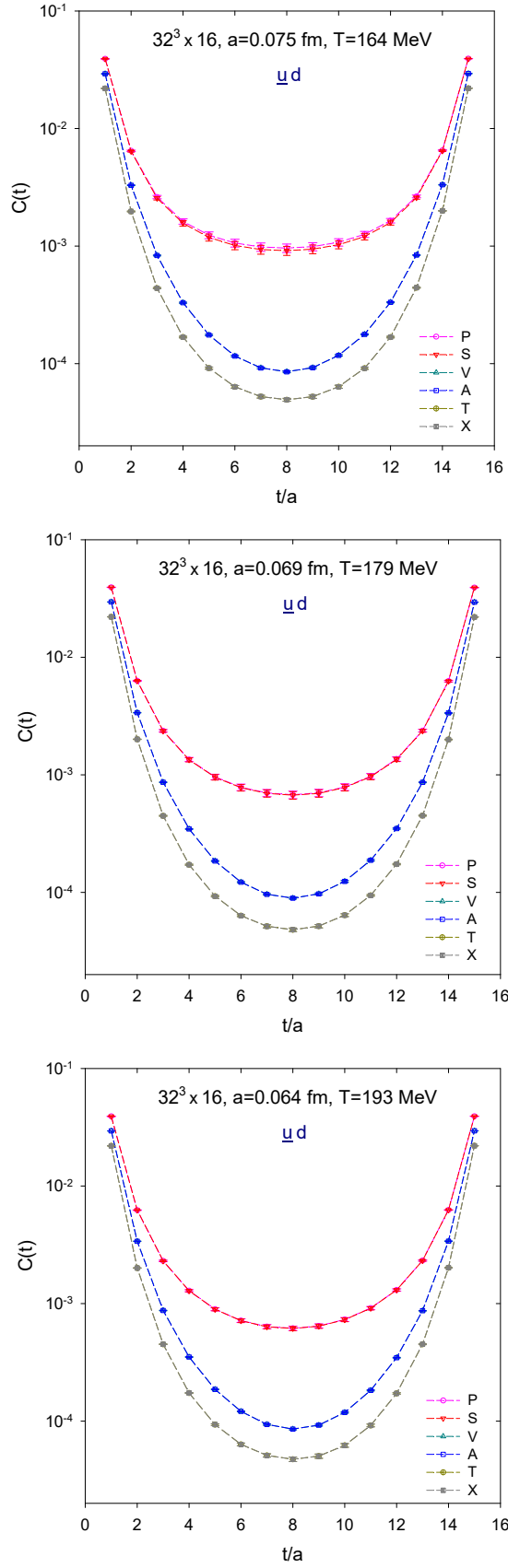


Figure 1: t -correlators of $\bar{u}\Gamma d$ at the three lowest temperatures. The dashed lines connecting the data points in each channel are shown only to guide the eye.

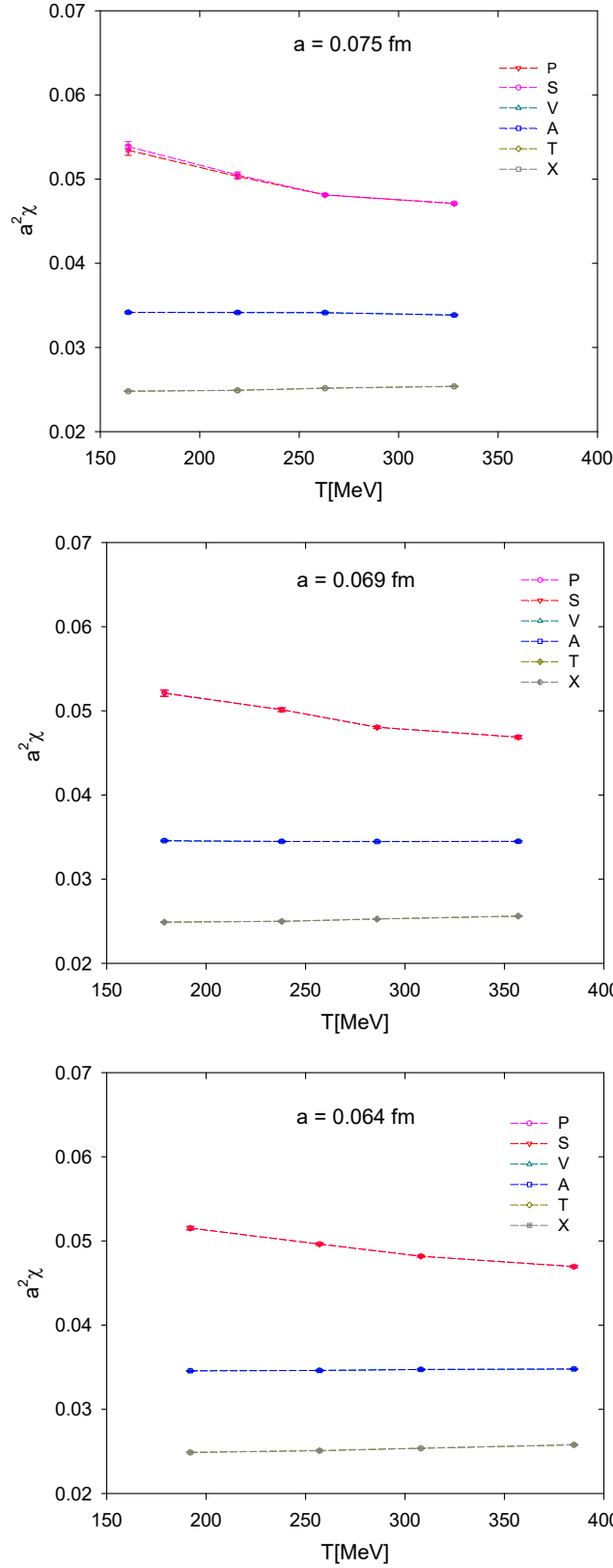


Figure 2: Regularized susceptibilities of $\bar{u}\Gamma d$ for three lattice spacings $a=(0.075, 0.069, 0.064)$ fm and twelve temperatures from 164-385 MeV. The dashed lines connecting the data points in each channel are shown only to guide the eye.

Accordingly, we compute the regularized susceptibilities $\chi_P, \chi_S, \chi_V, \chi_A, \chi_T$, and χ_X , shown in figure 2, as well as the RG-invariant symmetry ratios κ_{PS}, κ_{VA} , and κ_{TX} presented in figure 3. These quantities are obtained for three lattice spacings $a = (0.075, 0.069, 0.064)$ fm and twelve temperatures from 164 to 385 MeV.

Numerical values of the correlators, susceptibilities, and symmetry ratios are provided in appendix B.

In figure 2, the regularized susceptibilities show no splitting within any doublet, again except for the (P, S) channel at $T = 164$ MeV on the coarsest lattice. This aligns with the behavior seen in the correlators and reinforces the interpretation that the observed (P, S) deviations at the lowest temperature are artifacts of finite lattice spacing.

From figure 3, a clear hierarchy emerges:

$$\kappa_{PS} \gg \kappa_{TX} \simeq \kappa_{VA},$$

which holds for all three lattice spacings and across the entire temperature range. Note that the vertical scale for κ_{PS} (upper panel) is two orders of magnitude larger than those for κ_{VA} and κ_{TX} (lower panels). If one were to use κ_{PS} and κ_{VA} at finite a as measures of $U(1)_A$ and $SU(2)_L \times SU(2)_R$ breaking, respectively, the data would suggest that $U(1)_A$ restoration occurs at a higher temperature than chiral symmetry restoration. Conversely, using κ_{TX} as the $U(1)_A$ indicator would imply that both symmetries are restored at nearly the same temperature, even at finite spacing. This apparent contradiction can only be resolved by taking the continuum limit, which we address in the next section.

5 Continuum limit

After testing the data for $\kappa_{PS}(a, T)$, $\kappa_{VA}(a, T)$, and $\kappa_{TX}(a, T)$ against various models, we find that at fixed lattice spacing a , the temperature dependence of each κ can be well described by a simple power law:

$$\kappa(a, T) = A(a)(T[\text{GeV}])^{-B(a)}, \quad (5.1)$$

where the temperature T is expressed in GeV.

For each lattice spacing, we first extract the parameters $A(a)$ and $B(a)$ via a log-linear fit:

$$\ln \kappa(a, T) = \ln A(a) - B(a) \ln (T[\text{GeV}]).$$

The resulting fitted parameters $A(a)$ and $B(a)$, together with the corresponding χ^2/dof , are summarized for κ_{PS} , κ_{VA} , and κ_{TX} in the first three rows of table 3.

In the second step, we extrapolate $A(a)$ and $B(a)$ to the continuum limit ($a \rightarrow 0$). We consider both linear and exponential extrapolations in a^2 :

$$f(a) = f_0 + f_1 a^2, \quad \text{or} \quad f(a) = f_0 \exp(f_1 a^2),$$

and choose between them based on the behavior of the data. If a linear fit yields an unphysical $f_0 < 0$, we adopt the exponential form, which includes higher-order contributions

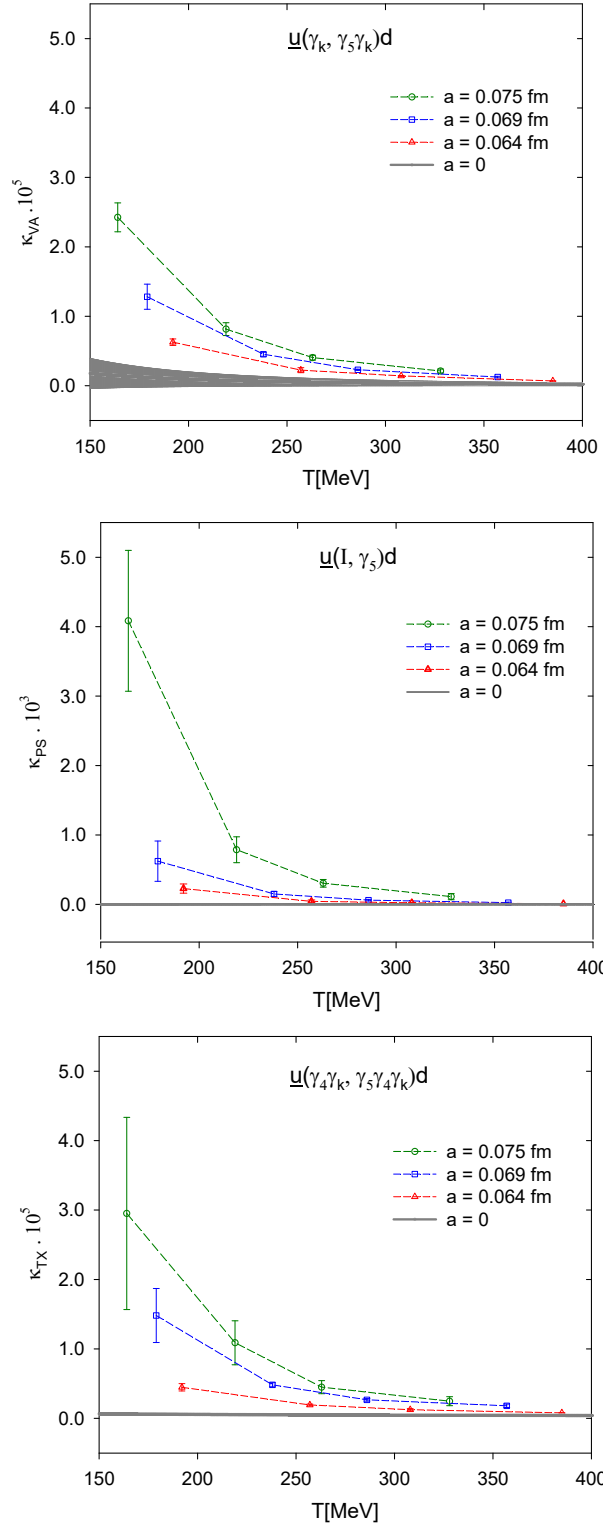


Figure 3: RG-invariant symmetry ratios κ_{VA} and $\{\kappa_{PS}, \kappa_{TX}\}$ for the $SU(2)_L \times SU(2)_R$ and $U(1)_A$ chiral symmetries of (u, d) quarks, computed at three lattice spacings $a = (0.075, 0.069, 0.064)$ fm and twelve temperatures in the range 164–385 MeV. The solid line and its band denote the continuum-extrapolated value and its uncertainty from 2D global fit.

a [fm]	κ_{PS}			κ_{VA}			κ_{TX}		
	$A \times 10^7$	B	χ^2/dof	$A \times 10^8$	B	χ^2/dof	$A \times 10^8$	B	χ^2/dof
0.075	2.53(2.08)	5.33(56)	0.13	3.38(1.03)	3.63(20)	0.54	3.85(3.63)	3.65(69)	0.28
0.069	2.19(1.92)	4.55(67)	0.13	3.34(89)	3.41(20)	1.45	7.43(3.62)	2.92(36)	1.31
0.064	1.04(83)	4.59(61)	0.34	3.29(37)	3.18(10)	0.26	8.21(1.24)	2.36(14)	0.79
cont. extrapol.	exp.	linear	χ^2/dof	linear	linear	χ^2/dof	linear	exp.	χ^2/dof
2-step	0.14(0.46)	2.64(2.42)	0.10, 0.25	3.08(2.60)	2.12(58)	< 0.1, < 0.1	17.66(9.17)	0.82(0.36)	0.10, < 0.1
2D	0.60(2.28)	1.47(2.79)	0.35	2.71(2.17)	2.20(48)	0.56	26.29(4.43)	0.47(0.11)	0.75

Table 3: Fitted parameters $A(a)$, $B(a)$, and χ^2/dof for the power-law ansatz $\kappa(a, T) = A(a)(T[\text{GeV}])^{-B(a)}$ for κ_{PS} , κ_{VA} , and κ_{TX} at three lattice spacings. The fourth row indicates the functional form (linear or exponential) used in the continuum extrapolation of $A(a)$ and $B(a)$ for the two-step fit and the two-dimensional global fit. The last two rows present the continuum results ($a = 0$) obtained via the two-step and 2D global fitting methods.

in a^2 and ensures positivity of f_0 . For cases where both forms are viable, we select the one that gives the better fit to the data. The requirement $f_0 > 0$ is physically motivated: $A_0 < 0$ would imply $\kappa(a = 0, T) < 0$, contradicting the definition $\kappa_{AB} \geq 0$ from Eq. (2.6), while $B_0 < 0$ would imply that κ increases with T , inconsistent with the expected decrease of $SU(2)_L \times SU(2)_R$ and $U(1)_A$ breakings as temperature rises.

The continuum-extrapolated parameters A_0 and B_0 , along with their χ^2/dof and the chosen fitting functions, are listed for κ_{PS} , κ_{VA} , and κ_{TX} in the last two rows of table 3.

Guided by the functional forms adopted in the two-step method (fourth row of table 3), we also perform a simultaneous two-dimensional (2D) global fit to all 12 data points of each $\kappa_{AB}(a, T)$ using one of the following models:

$$\kappa(a, T) = (A_0 + A_1 a^2)(T[\text{GeV}])^{-(B_0 + B_1 a^2)}, \quad (5.2)$$

$$\kappa(a, T) = A_0 \exp(A_1 a^2)(T[\text{GeV}])^{-(B_0 + B_1 a^2)}, \quad (5.3)$$

$$\kappa(a, T) = (A_0 + A_1 a^2)(T[\text{GeV}])^{-B_0 \exp(B_1 a^2)}, \quad (5.4)$$

where Eq. (5.3) is used for $\kappa_{PS}(a, T)$, Eq. (5.2) for $\kappa_{VA}(a, T)$, and Eq. (5.4) for $\kappa_{TX}(a, T)$.

The resulting continuum parameters A_0 and B_0 and the corresponding χ^2/dof are given in the last row of table 3. The values obtained from the 2D global fit are consistent with those from the two-step method.

Statistically, the 2D-fit is more reliable because it performs a simultaneous minimization over the entire dataset, which ensures a globally optimized balance between parameters A and B , and generally yields a better χ^2 per degree of freedom. In contrast, the 2-step fit first fits each a -group independently to obtain local estimates $A(a)$ and $B(a)$, then performs a secondary regression on those results. This "fit-of-fits" approach propagates errors less efficiently and can introduce bias if a particular a -group exhibits larger statistical fluctuations. Such behavior is evident in table 3, where the $\chi^2/\text{d.o.f.}$ values of κ_{VA} and κ_{TX} at $a = 0.069$ fm are significantly larger than those at other lattice spacings.

$T[\text{MeV}]$	$\kappa_{PS}(a=0)$	$\kappa_{VA}(a=0)$	$\kappa_{TX}(a=0)$
150	$(9.7 \pm 63.2) \times 10^{-7}$	$(1.77 \pm 2.15) \times 10^{-6}$	$(6.42 \pm 1.68) \times 10^{-7}$
164	$(8.5 \pm 53.8) \times 10^{-7}$	$(1.46 \pm 1.73) \times 10^{-6}$	$(6.16 \pm 1.57) \times 10^{-7}$
179	$(7.5 \pm 45.8) \times 10^{-7}$	$(1.20 \pm 1.39) \times 10^{-6}$	$(5.91 \pm 1.47) \times 10^{-7}$
219	$(5.6 \pm 31.7) \times 10^{-7}$	$(7.69 \pm 8.36) \times 10^{-7}$	$(5.37 \pm 1.25) \times 10^{-7}$
257	$(4.4 \pm 23.6) \times 10^{-7}$	$(5.41 \pm 5.60) \times 10^{-7}$	$(4.98 \pm 1.10) \times 10^{-7}$
385	$(2.4 \pm 11.3) \times 10^{-7}$	$(2.22 \pm 2.05) \times 10^{-7}$	$(4.12 \pm 0.81) \times 10^{-7}$

Table 4: Continuum extrapolated values of κ_{PS} , κ_{VA} , and κ_{TX} at selected temperatures between 150 and 400 MeV.

We therefore adopt the 2D-fit results for A_0 and B_0 to obtain the continuum-extrapolated κ_{PS} , κ_{VA} , and κ_{TX} . These are shown as solid curves in Fig. 3, with the error bands indicating the uncertainty. Note that the vertical scale for κ_{PS} (upper panel) is two orders of magnitude larger than those for κ_{VA} and κ_{TX} (lower panels). The continuum extrapolated values of κ_{PS} , κ_{VA} and κ_{TX} are compatible with one another across the temperature range 150–400 MeV, within our precision. This is illustrated explicitly in table 4, which lists the continuum values at several representative temperatures.

6 Discussion and Outlook

In this work, we have introduced a renormalization-group invariant observable, the symmetry strength parameter κ_{AB} , designed to provide a quantitative and scheme-independent measure of symmetry breaking in QCD. Using this ratio, we have performed a systematic lattice study of the relative strength of $SU(2)_L \times SU(2)_R$ chiral symmetry breaking and $U(1)_A$ axial symmetry breaking in finite-temperature QCD with $N_f = 2 + 1 + 1$ flavors, employing optimal domain-wall fermions at the physical point. Our analysis spans three lattice spacings and twelve temperatures in the range 164–385 MeV, allowing for controlled continuum extrapolations across the chiral crossover region.

We examined three independent symmetry-breaking channels in the *nonsinglet sector with connected correlators*, namely: the scalar–pseudoscalar channel sensitive to $U(1)_A$ breaking (κ_{PS}), the vector–axial–vector channel probing chiral symmetry breaking (κ_{VA}), and an additional $U(1)_A$ -sensitive tensor–axial–tensor channel (κ_{TX}). At finite lattice spacing, these channels exhibit a clear hierarchy: $\kappa_{PS} > \kappa_{TX} \sim \kappa_{VA}$. However, this hierarchy collapses in the continuum limit, where all three symmetry strength parameters become statistically indistinguishable within our current precision.

This degeneracy constitutes a robust, model-independent result obtained from a chirally symmetric lattice formulation and demonstrates that discretization effects play a central role in apparent differences among symmetry-breaking channels. From a physical perspective, our findings indicate that chiral and axial symmetry-breaking effects for the *nonsinglet* sector in QCD become comparably suppressed over a narrow temperature interval near the chiral crossover. We find no evidence for a parametrically separated restoration scale for $U(1)_A$ symmetry relative to $SU(2)_L \times SU(2)_R$ symmetry in the continuum limit—a

result that places stringent quantitative constraints on phenomenological descriptions of finite-temperature QCD that rely on delayed axial symmetry restoration.

Within a renormalization-group framework, the observed continuum-limit degeneracy of κ_{PS} , κ_{VA} , and κ_{TX} implies that $SU(2)_L \times SU(2)_R$ and $U(1)_A$ symmetry-breaking effects for *connected correlators* become comparably suppressed near T_c . This suggests that the corresponding symmetry-breaking operators acquire similar infrared relevance for non-singlet observables. However, as we discuss in section 6.1, the full effective restoration pattern—including singlet channels—reveals a more intricate structure that refines simple RG scenarios based solely on nonsinglet data.

6.1 Connections to topological susceptibility and singlet sector

An important subtlety involves the disconnected parts of the scalar singlet (σ) and pseudoscalar singlet (η) mesons in $N_f = 2$ QCD. Recall that the physical η' corresponds to the η singlet in $N_f = 2$ QCD. Upon effective restoration of *full* $SU(2)_L \times SU(2)_R$ chiral symmetry, i.e., satisfaction of Eqs. (2.11), (2.7) and (2.8), the latter two equations involving both nonsinglet and singlet channels yield

$$\chi_\sigma - \chi_\delta = \chi_\pi - \chi_\delta = \chi_\pi - \chi_\eta, \quad (6.1)$$

which relates the disconnected parts of χ_σ and χ_η :

$$\chi_{\text{disc}} \equiv \chi_\sigma - \chi_\delta = \chi_\pi - \chi_\eta \equiv \chi_{5,\text{disc}}, \quad (6.2)$$

where

$$\chi_{\text{disc}} = \frac{1}{V} \left\{ \langle [\text{Tr}(D_c + m_q)^{-1}]^2 \rangle - \langle \text{Tr}(D_c + m_q)^{-1} \rangle^2 \right\}, \quad (6.3)$$

$$\chi_{5,\text{disc}} = \frac{1}{V} \left\{ \langle [\text{Tr}\gamma_5(D_c + m_q)^{-1}]^2 \rangle - \langle \text{Tr}\gamma_5(D_c + m_q)^{-1} \rangle^2 \right\}. \quad (6.4)$$

In lattice QCD with exact chiral symmetry, the topological charge Q_t satisfies

$$Q_t = m_q \text{Tr}\gamma_5(D_c + m_q)^{-1}, \quad \forall m_q > 0. \quad (6.5)$$

Assuming Eq. (6.5) can be measured precisely (e.g., with overlap fermions via index theorem), Eq. (6.2) implies

$$\chi_{\text{disc}} = \chi_{5,\text{disc}} = \frac{\chi_t}{m_q^2}, \quad (6.6)$$

where χ_t is the topological susceptibility,

$$\chi_t = \frac{1}{V} (\langle Q_t^2 \rangle - \langle Q_t \rangle^2). \quad (6.7)$$

Thus, upon effective restoration of *full* $SU(2)_L \times SU(2)_R$ chiral symmetry, χ_t/m_q^2 equals any of the three differences: $\chi_\sigma - \chi_\delta$, $\chi_\pi - \chi_\delta$, or $\chi_\pi - \chi_\eta$. However, Eq. (6.1) presents a puzzle: how could $(\chi_\pi - \chi_\delta)$, which involves only connected correlators, equal $\chi_{\text{disc}} = \chi_t/m_q^2$, which arises solely from disconnected diagrams? This puzzle is resolved by considering the effective

restoration of *full* $U(1)_A$ axial symmetry, which requires both Eq. (2.12) (nonsinglet) and Eq. (2.13) (singlet) to be satisfied. Subtracting Eq. (2.12) from Eq. (2.13) gives

$$\chi_\sigma - \chi_\delta = \chi_\eta - \chi_\pi, \quad (6.8)$$

which contradicts Eq. (6.1) unless all susceptibility differences in both equations vanish—implying $\chi_t = 0$. In other words, *full* effective restoration of both $SU(2)_L \times SU(2)_R$ and $U(1)_A$ symmetries requires vanishing topological susceptibility.

This leads to a natural *two-stage hierarchical effective restoration* scenario illustrated in Fig. 4:

- **Stage 1** ($T \sim T_c^{ns} \simeq T_c \sim 156$ MeV): Effective restoration of both $SU(2)_L \times SU(2)_R$ and $U(1)_A$ symmetries in the *nonsinglet* sector, where connected correlators become degenerate:

$$- U(1)_A: \chi_\pi \approx \chi_\delta \text{ (Eq. 2.12)}, \chi_{\rho_T} \approx \chi_{b_1} \text{ (Eq. 2.14)}$$

$$- SU(2)_L \times SU(2)_R: \chi_\rho \approx \chi_{a_1} \text{ (Eq. 2.11)}$$

- **Stage 2** ($T \sim T_c^s \gg T_c^{ns}$): Full effective restoration including *singlet* and *mixed singlet-nonsinglet* channels, requiring $\chi_t \rightarrow 0$, $\kappa_{\omega_T, h_{1T}} \rightarrow 0$ and satisfaction of all relations (eqs. (2.7)–(2.15)) including eqs. (6.1) and (6.8):

$$- SU(2)_L \times SU(2)_R: \chi_\sigma = \chi_\pi, \chi_\eta = \chi_\delta, \chi_{\omega_T} = \chi_{b_1}, \chi_{h_{1T}} = \chi_{\rho_T}$$

$$- U(1)_A: \chi_\sigma = \chi_\eta, \chi_{\omega_T} = \chi_{h_{1T}}$$

In this picture, $\chi_\pi - \chi_\delta$ (probing nonsinglet $U(1)_A$ restoration) is distinct from $\chi_\sigma - \chi_\delta$ and $\chi_\pi - \chi_\eta$ (probing mixed singlet-nonsinglet channel restoration). The former can approach zero while the latter remain finite, reflecting the persistence of topological fluctuations. The key insight is that *both* $SU(2)_L \times SU(2)_R$ and $U(1)_A$ symmetries exhibit *two-stage restoration*: they first restore in the nonsinglet sector around $T_c^{ns} \sim 156$ MeV, and only later restore fully (including singlet channels) at a much higher temperature $T_c^s \gg T_c^{ns}$ when topological fluctuations are largely suppressed ($\chi_t \rightarrow 0$).

6.2 Hierarchical restoration of chiral and axial symmetries

Our analysis of κ_{PS} , κ_{VA} , and κ_{TX} provides direct evidence for Stage 1 (nonsinglet restoration) of this hierarchical restoration. The near-vanishing of κ_{PS} and κ_{TX} around T_c demonstrates that $U(1)_A$ -anomaly effects on *connected correlators* become negligible in this regime, signaling effective $U(1)_A$ restoration in the nonsinglet sector. Similarly, $\kappa_{VA} \rightarrow 0$ indicates effective $SU(2)_L \times SU(2)_R$ restoration in the nonsinglet sector.

This hierarchical picture explains the apparent tension between different lattice studies. In the nonsinglet sector ($T \sim T_c^{ns} \sim 156$ MeV), both $SU(2)_L \times SU(2)_R$ and $U(1)_A$ symmetries effectively restore for connected channels as thermal screening reduces instanton effects on chiral partner splittings (π - δ , ρ - a_1 , ρ_T - b_1). Conversely, full effective restoration ($T \sim T_c^s \gg T_c^{ns}$) including singlet channels requires $\chi_t \rightarrow 0$ and $\kappa_{\omega_T, h_{1T}} \rightarrow 0$, which occur at significantly higher temperatures.

Two-Stage Hierarchical Restoration (Effective)

Stage 2: Full Effective Restoration at $T = T_c^s \gg T_c^{\text{ns}}$

Criterion: $\kappa_{\omega_T, h_{1T}} = 0$, and $\chi_t = 0$ (**within errors**)

$SU(2)_L \times SU(2)_R$ (s+ns): $\chi_\sigma = \chi_\pi$, $\chi_\eta = \chi_\delta$, $\chi_{\omega_T} = \chi_{b_1}$, $\chi_{h_{1T}} = \chi_{\rho_T}$

$U(1)_A$ (s): $\chi_\sigma = \chi_\eta$, $\chi_{\omega_T} = \chi_{h_{1T}}$

$\uparrow \chi_t, \kappa_{\omega_T, h_{1T}} \rightarrow 0$

Stage 1: Effective Restoration (Nonsinglet) at $T = T_c^{\text{ns}} \sim 156$ MeV

Criterion: $\kappa_{PS}, \kappa_{VA}, \kappa_{TX} = 0$ (**within errors**)

$SU(2)_L \times SU(2)_R$ (ns): $\chi_\rho = \chi_{a_1}$

$U(1)_A$ (ns): $\chi_\pi = \chi_\delta$, $\chi_{\rho_T} = \chi_{b_1}$

Temperature scale: $T_c^{\text{ns}} \sim 156$ MeV (Stage 1) \longrightarrow $T_c^s \gg T_c^{\text{ns}}$ (Stage 2, threshold-dependent)

Observables (RG-invariant κ_{AB} in the continuum limit):

κ_{PS} : π - δ (nonsinglet $U(1)_A$, scalar, connected)

κ_{VA} : ρ - a_1 (nonsinglet $SU(2)_L \times SU(2)_R$, vector, connected)

κ_{TX} : ρ_T - b_1 (nonsinglet $U(1)_A$, tensor, connected)

$\kappa_{\omega_T, h_{1T}}$: ω_T - h_{1T} (singlet $U(1)_A$, tensor, **Stage 2 probe**)

$\kappa(\chi_{\omega_T}, \chi_{b_1})$: ω_T - b_1 (singlet-nonsinglet $SU(2)_L \times SU(2)_R$, tensor, **Stage 2 probe**)

$\kappa(\chi_{h_{1T}}, \chi_{\rho_T})$: h_{1T} - ρ_T (singlet-nonsinglet $SU(2)_L \times SU(2)_R$, tensor, **Stage 2 probe**)

χ_t : topological susceptibility (**Stage 2 probe**)

Neither stage implies exact restoration; both are

operational thresholds defined by $\kappa_{AB} = 0$ within errors.

Figure 4: Schematic illustration of the two-stage hierarchical restoration scenario for light (u, d) quarks. Stage 1 (nonsinglet restoration) occurs around $T_c^{\text{ns}} \sim 156$ MeV, while Stage 2 (full effective restoration including singlets) requires $\chi_t \rightarrow 0$ and $\kappa_{\omega_T, h_{1T}} \rightarrow 0$ at a much higher temperature $T_c^s \gg T_c^{\text{ns}}$. The κ_{AB} ratios for nonsinglet channels (κ_{PS} , κ_{VA} , κ_{TX}) probe Stage 1, while tensor singlet and mixed singlet-nonsinglet tensor ratios ($\kappa_{\omega_T, h_{1T}}$, $\kappa(\chi_{\omega_T}, \chi_{b_1})$, $\kappa(\chi_{h_{1T}}, \chi_{\rho_T})$) and direct χ_t measurements probe Stage 2.

For $N_f = 2+1+1$ QCD at the physical point, the chiral transition is a smooth crossover. Consequently, $\chi_\sigma - \chi_\delta$ or $\chi_\eta - \chi_\pi$ never vanishes identically but gradually diminishes as T increases above $T_c \sim T_c^{\text{ns}}$. The relation $\chi_\sigma^R - \chi_\delta^R = \chi_t/m_q^2$ is obscured in practice by lattice artifacts, residual chiral symmetry breaking, anomalous renormalization uncertainties, and the inherent nonzero difference in a crossover. Lattice determinations of $\chi_t(T)$ suffer from significant discretization artifacts, and a consistent continuum picture has not yet emerged across different studies (see e.g., [39, 45–48]). In general, for $N_f = 2+1$ and $N_f = 2+1+1$ QCD at physical masses, $\chi_t(T)$ remains sizeable up to $T \gg T_c$, indicating that topological fluctuations are not fully suppressed until well above the chiral crossover.

Notably, in lattice QCD with exact chiral symmetry, $\chi_t(T)$ for physical $N_f = 2+1$ and $N_f = 2+1+1$ QCD can be much larger than that of $N_f = 2$ QCD in the chiral limit (see appendix A of ref. [49]). This raises an intriguing possibility: in the $N_f = 2$ chiral limit, the two-stage hierarchy might nearly collapse, with $T_c^s \gtrsim T_c^{\text{ns}} \sim T_c$, implying that full effective restoration (including singlet channels) could occur much closer to the chiral transition

temperature. Our simulations at physical masses cannot address this scenario directly, as the strange and charm quarks explicitly break the symmetry and enhance topological fluctuations.

Our κ_{PS} , κ_{VA} , and κ_{TX} measurements, being ratios, cancel many systematics and cleanly show the trend toward symmetry restoration in the nonsinglet sector. The persistence of $\chi_t > 0$ for $T \gtrsim T_c$ in lattice studies is therefore not in tension with $\kappa_{PS}, \kappa_{VA}, \kappa_{TX} \rightarrow 0$; rather, it reflects the hierarchy $T_c^{ns} \approx T_c < T_c^s$. The anomaly thus influences different observables in distinct ways and on different temperature scales. While χ_t probes the global topological charge distribution and remains finite until much higher temperatures (falling off with a power-law consistent with dilute instanton gas prediction [50], although the overall normalization may differ significantly), nonsinglet meson correlators are sensitive primarily to the *anomaly-induced splitting* within chiral partners—a splitting that can diminish due to thermal screening even while topological fluctuations themselves persist.

Probing full effective restoration with tensor singlet channels While κ_{PS} , κ_{VA} , and κ_{TX} cleanly signal nonsinglet restoration near T_c^{ns} , the singlet sector remains numerically challenging. As discussed in section 2.4, the tensor singlet operators $\omega_{T,k} \equiv T_k^s = \bar{q}\gamma_4\gamma_k q$ and $h_{1T,k} \equiv X_k^s = \bar{q}\gamma_5\gamma_4\gamma_k q$ offer a theoretically cleaner alternative to scalar/pseudoscalar singlets. For chirally symmetric fermions, their renormalization constants satisfy $Z_T^s = Z_X^s$, and after contact term and vacuum subtraction, their susceptibilities are multiplicatively renormalizable with the same factor $(Z_T^s)^2$, ensuring that $\kappa_{TX}^s = (\chi_T^s - \chi_X^s)/(\chi_T^s + \chi_X^s)$ is RG-invariant. Measuring this ratio in future studies will therefore provide a direct probe of *full $U(1)_A$ effective restoration in the singlet sector*. If the hierarchical picture is correct, $\kappa_{\omega_T, h_{1T}}$ should remain non-zero well above T_c^{ns} and approach zero only at a higher temperature $T_c^s \gg T_c^{ns}$.

6.3 Broader symmetry landscape and emergent phases above T_c

The hierarchical picture presented above aligns with growing evidence for multi-stage transitions above T_c . Beyond the familiar $SU(2)_L \times SU(2)_R$ and $U(1)_A$ symmetries, recent lattice studies reveal emergent approximate symmetries absent in the classical QCD Lagrangian. In particular, approximate chiral-spin $SU(2)_{CS}$ symmetry [51] observed in $N_f = 2$ [52, 53], $N_f = 2 + 1 + 1$ [25, 31], and $N_f = 2 + 1 + 1 + 1$ [32] lattice QCD indicates that hadron-like states bound predominantly by chromoelectric interactions persist well above T_c .

It is important to distinguish this emergent symmetry from the usual chiral symmetries. For $SU(2)_L \times SU(2)_R$ and $U(1)_A$, symmetry breaking decreases monotonically with temperature, and the symmetries themselves become effectively restored as partner degeneracy improves. These symmetries are always present in the Lagrangian — only their breaking weakens.

In contrast, $SU(2)_{CS}$ chiral-spin symmetry is not present in the QCD Lagrangian. It emerges only in an intermediate window where chromoelectric binding dominates, typically from $T \sim 2T_c$ up to $T \sim 4T_c$ for light (u, d) quarks. The window boundaries depend on two thresholds: ϵ_{CS} for emergence at T_{CS} , and ϵ_{CSF} for fading at $T_{CSF} > T_{CS}$. Within this window, $SU(2)_{CS}$ breaking decreases with T , allowing hadron-like states bound by

chromoelectric interactions to exist. As temperature increases, thermal excitation energy eventually exceeds the chromoelectric binding energy, leading to quark deconfinement. This is manifested when one $SU(2)_{\text{CS}}$ multiplet (V_k, T_k, X_k) merges with the (P, S) multiplet of $U(1)_A$ symmetry, leaving only the usual chiral symmetries relevant. At this point, chiral-spin symmetry *fades away* — not simply becoming more broken, but physically disappearing due to thermal excitations.

Similarly, the observation of an infrared symmetric phase [54] around $T_{\text{IR}} \sim 230$ MeV in $N_f = 2 + 1$ lattice QCD [55], which disappears by $T \gtrsim 300$ MeV, supports a correlated, quasi-hadronic medium in the window $T_c \lesssim T \lesssim 2T_c$. In this regime, hadrons become progressively delocalized, forming a dense fluid where both chromoelectric and chromomagnetic interactions remain active. The usual chiral multiplets are already restored in the nonsinglet sector, but chiral-spin symmetry is not yet manifest.

The gradual loss of binding across both regimes is consistent with the observed reduction in $U(1)_A$ -breaking effects in connected channels (as measured by κ_{PS} and κ_{TX}), while topological fluctuations—including center vortices [56] and instanton-like objects—remain active until higher temperatures.

These emergent symmetry patterns are complemented by topological studies. Center-vortex analyses in $N_f = 2 + 1$ QCD observe a pronounced change in vortex percolation at approximately $\gtrsim 2T_c$ [57]. While vortex density drops substantially, a sparse network survives to higher temperatures, reinforcing that topological fluctuations — intimately connected to the $U(1)_A$ anomaly — remain non-negligible well into the deconfined regime. This provides a plausible mechanism for continued $U(1)_A$ breaking where nonsinglet chiral symmetry is largely restored. The smooth crossover implies no sharp “complete deconfinement” point; instead, the system evolves gradually from hadronic to quark–gluon plasma, with residual correlations possible even at $T \gg 2T_c$.

Taken together, these independent lines of evidence support the two-stage effective restoration scenario described in section 6.1. Stage 1 ($T \sim T_c^{ns}$) is characterized by effective restoration of nonsinglet symmetries, as demonstrated by the vanishing of κ_{PS} , κ_{VA} , and κ_{TX} in this work. Stage 2 ($T \sim T_c^s$) involves full effective restoration of singlet channels and suppression of topological fluctuations ($\chi_t \rightarrow 0$). Consistent comparison between lattice studies requires continuum extrapolation of each observable, as demonstrated here. Since the chiral transition at physical quark masses is a smooth crossover, any symmetry-breaking observable decreases gradually with temperature. The Stage 2 scenario remains to be conclusively established through future continuum-extrapolated measurements of tensor-singlet ratios and topological susceptibility.

6.4 Future computational improvements and extensions

6.4.1 Computational improvements and tensor singlet probes

To build upon this work, several computational improvements are planned:

- **Continuum extrapolation:** We will perform simulations at several fixed temperatures, each with multiple lattice spacings to reduce systematic uncertainties in the continuum extrapolation of κ_{PS} , κ_{VA} , and κ_{TX} .

- **Finite-volume effects:** We will employ lattices with larger spatial volumes (40^3 and 64^3) to better distinguish between finite-size artifacts and genuine thermodynamic behavior.
- **Statistical precision:** We will increase the number of gauge configurations in each ensemble to reduce statistical uncertainties in correlation function measurements.
- **Flavor-singlet tensor channels:** Using stochastic all-to-all propagators with color–Dirac dilution, we will compute the singlet tensor (ω_T) and axial-tensor (h_{1T}) susceptibilities. The tensor singlet ratio

$$\kappa_{\omega_T, h_{1T}} \equiv \frac{\chi_{\omega_T} - \chi_{h_{1T}}}{\chi_{\omega_T} + \chi_{h_{1T}}},$$

where $\omega_{T,k} = \bar{q}\gamma_4\gamma_k q$ and $h_{1T,k} = \bar{q}\gamma_5\gamma_4\gamma_k q$, provides a theoretically clean (power-divergence free) probe of $U(1)_A$ restoration in the **singlet sector**. This will enable a direct test of the two-stage $U(1)_A$ restoration scenario at $T_c^s \gg T_c^{ns}$.

- **Mixed singlet–nonsinglet channels:** The mixed ratios $\kappa(\chi_{\omega_T}, \chi_{b_1})$ and $\kappa(\chi_{h_{1T}}, \chi_{\rho_T})$ probe $SU(2)_L \times SU(2)_R$ restoration between singlet and nonsinglet tensor operators, offering additional insight into the chiral symmetry realization pattern across singlet and nonsinglet flavor sectors.

6.4.2 Extension to flavor-singlet channels

Beyond the flavor-nonsinglet mesons studied here, the restoration patterns of $SU(2)_L \times SU(2)_R$ chiral symmetry and $U(1)_A$ axial symmetry can also be probed through flavor-singlet meson channels. To verify consistency in the continuum limit, we will evaluate all-to-all quark propagators using stochastic estimation. The stochastic sources will be constructed with Z_2 noise vectors, diluted in both color and Dirac space. Specifically, each noise vector will have support on a single color–Dirac component (3×4 in total), with entries randomly chosen as ± 1 . This dilution scheme reduces off-diagonal contamination and improves the signal-to-noise ratio. A practical challenge lies in controlling statistical uncertainties for disconnected diagrams. We will explore advanced variance-reduction techniques to achieve sufficient precision for the flavor-singlet channels, alongside direct measurements of χ_t using the overlap operator and index theorem to comprehensively map the symmetry restoration landscape.

6.5 RG interpretation and comparison with Pisarski–Wilczek analyses

The renormalization-group analysis of Pisarski–Wilczek (PW) [14] shows that the order of the two-flavor chiral transition is controlled by the RG scaling of the $U(1)_A$ -breaking operator at the $O(4)$ fixed point. If this operator is *relevant*, axial symmetry remains broken and the infrared flow is governed by the stable $O(4)$ Wilson–Fisher fixed point, allowing a *second-order transition in the $O(4)$ universality class*. If it is *irrelevant*, the effective symmetry enlarges to $U(2)_L \times U(2)_R$; the ϵ -expansion of the corresponding Landau–Ginzburg

theory reveals *no infrared-stable fixed point*, implying runaway RG flow and a *fluctuation-induced first-order transition*.

The PW scenario applies strictly to the *chiral limit* ($m_q = 0$) at the exact infrared critical fixed point and therefore characterizes *universality classes*, rather than specific observables at finite quark mass. In physical QCD with $m_q \neq 0$, where the transition is a smooth crossover and no true critical fixed point exists, axial symmetry restoration must be defined operationally. In this work, we define “effective restoration” through the vanishing of the κ_{AB} ratio within statistical uncertainties (section 2.3). This condition is substantially weaker than the RG irrelevance criterion of PW: it does not imply enlargement of the symmetry to $U(2)_L \times U(2)_R$ or a change in universality class, but only that symmetry-breaking effects are not resolved within the present observables and statistical precision.

With this distinction, our results reveal a **two-stage pattern of operational symmetry restoration**.

Stage 1 (nonsinglet sector): Near $T_c^{\text{ns}} \sim 156$ MeV, the ratios κ_{PS} , κ_{VA} , and κ_{TX} become consistent with zero, indicating operational effective restoration of $SU(2)_L \times SU(2)_R$ and $U(1)_A$ in the nonsinglet sector. However, this temperature does not correspond to the critical temperature of the PW framework, which refers to the chiral limit and requires restoration of full chiral symmetry at the infrared fixed point. Since singlet channels remain nondegenerate, the universality-class arguments of PW do not directly apply at this stage.

Stage 2 (singlet sector): At a significantly higher temperature $T_c^{\text{s}} \gg T_c^{\text{ns}}$, the singlet ratio $\kappa_{\omega_T, h_{1T}}$ and the topological susceptibility χ_t also become consistent with zero, extending operational effective restoration to both singlet and nonsinglet sectors. This defines a more complete restoration scale than the PW critical temperature, which is determined solely by chiral symmetry in the massless limit and does not require observable axial degeneracy. Nevertheless, even at T_c^{s} , this operational restoration does not by itself establish enlargement of the symmetry to $U(2)_L \times U(2)_R$ or determine the universality class, as explicit symmetry-breaking effects from finite quark masses and the anomaly remain present in the Lagrangian. Rather, T_c^{s} marks the temperature at which symmetry breaking becomes unresolvable in all measured channels, representing a stronger phenomenological restoration scale beyond the strict RG definition of criticality.

Pisarski and Wilczek (PW) [14] identified two scenarios depending on whether the $U(1)_A$ -breaking operator is relevant or irrelevant at the $O(4)$ fixed point, with the latter implying enlargement of the symmetry to $U(2)_L \times U(2)_R$ and a fluctuation-induced first-order transition. The subsequent renormalization-group analysis of Pelissetto and Vicari (PV) [58] established that for $N_f = 2$ this operator is marginally irrelevant at the $O(4)$ fixed point, implying approximate $O(4)$ scaling in the chiral limit near the PW critical temperature. Our results differ qualitatively from this scenario. At $T_c^{\text{ns}} \sim 156$ MeV, we observe degeneracy in nonsinglet channels while singlet observables and the topological susceptibility remain nonvanishing, revealing a two-stage hierarchy of operational restoration. This structure does not follow from the fixed-point analysis, which applies strictly in the chiral limit and does not distinguish connected and disconnected contributions. Moreover, our temperatures T_c^{ns} and T_c^{s} are crossover scales in physical QCD rather than critical points, and the persistence of $\chi_t > 0$ reflects the continued contribution of disconnected diagrams

and the mass-dependent amplification of axial-anomaly effects. Thus, while marginal irrelevance provides an important conceptual backdrop, the hierarchical restoration observed here represents a distinct finite-mass phenomenon beyond the scope of the chiral-limit RG framework.

This interpretation is supported by complementary lattice studies probing chiral symmetry restoration from different perspectives. In the $N_f = 2$ chiral limit, continuum-controlled simulations using a many-flavor approach find that the apparent first-order behavior on coarse lattices is a discretization artifact, with the continuum transition consistent with second order and compatible with $O(N)$ scaling [59]. At the physical point in $N_f = 2 + 1 + 1$ QCD, independent scaling analysis with twisted-mass Wilson fermions [60] shows quantitative agreement with 3D $O(4)$ scaling over a broad temperature range, indicating that approximate critical scaling emerges already at nonzero quark mass.

Within this framework, our κ_{AB} observables provide the first continuum-extrapolated, quantitative evidence for **Stage 1**, namely the operational restoration of $SU(2)_L \times SU(2)_R$ and $U(1)_A$ in the nonsinglet (connected) sector near T_c . It is worth noting that other ratios such as $\kappa_{\sigma,\pi}$ and $\kappa_{\eta,\delta}$, which involve singlet channels, are also formally RG-invariant, as the underlying renormalization constants satisfy $Z_S^{ns} = Z_P^{ns} = Z_S^s = Z_P^s$ (see section 2.4). However, in practice, even after contact term and vacuum subtractions, the singlet susceptibilities χ_σ and χ_η retain finite mixing with the topological susceptibility χ_t , which must be disentangled to obtain fully renormalized quantities. This additional complication, together with the noise from disconnected diagrams, makes these ratios less accessible in the present study.

Together, these results support a coherent picture in which the axial anomaly becomes progressively less visible near the chiral crossover. The chiral-limit studies establish the relevance of $O(N)$ -type critical behavior at the true fixed point, while physical-mass simulations demonstrate that approximate $O(4)$ -like scaling and chiral partner degeneracy appear as precursor phenomena. Our observation of nonsinglet degeneracy near T_c^{ns} is consistent with this framework, while the delayed restoration in singlet channels reveals additional finite-mass and anomaly-driven effects beyond the strict chiral-limit universality-class description.

Functional renormalization-group analyses of $(2+1)$ -flavor QCD [61] similarly find that axial-anomaly effects persist throughout a broad crossover region. While nonsinglet observables exhibit degeneracy patterns consistent with approximate $O(4)$ -like symmetry, singlet channels remain sensitive to anomaly-driven disconnected contributions. As a result, the fully symmetric $U(2)_L \times U(2)_R$ scenario—requiring both $m_q = 0$ and exact irrelevance of axial breaking at the infrared fixed point—is not realized at the physical crossover temperature and is therefore not directly applicable to our simulation. Instead, the system follows a hierarchical restoration pattern consistent with our two-stage picture.

Establishing **Stage 2**, corresponding to full operational restoration including singlet channels, requires both $\kappa_{\omega_T, h_{1T}} \rightarrow 0$ and $\chi_t \rightarrow 0$ within uncertainties. Existing lattice studies show that topological fluctuations persist up to $T \gtrsim 2T_c$ (see e.g., [39, 45–48]), indicating that anomaly effects remain active well above the crossover. However, a definitive continuum-limit determination combining chirally symmetric fermions and overlap-based topology measurements for both sea and valence sectors is still lacking. Such calculations are

necessary to determine whether and at what temperature full effective restoration occurs.

Importantly, our results do not contradict the PW analysis, but instead probe a different regime. The PW framework applies strictly to the chiral limit at the infrared critical fixed point, where universal $O(4)$ scaling would govern all channels. By contrast, our study concerns physical QCD with nonzero quark masses, where symmetry restoration occurs through a crossover rather than a true critical transition. The observed degeneracy of nonsinglet chiral partners near T_c is a necessary precursor for $O(4)$ -like scaling, but does not by itself establish the associated universality class. The behavior of the singlet sector—and whether its eventual operational restoration at T_c^s bears any connection to the $U(2)_L \times U(2)_R$ scenario considered in the chiral-limit analysis—remains an open question. Future continuum-extrapolated measurements of κ_{TX}^s will directly probe the anomaly’s role in the singlet sector and further constrain the underlying symmetry-restoration mechanism.

6.6 Concluding remarks

The symmetry-strength parameter κ_{AB} introduced here provides a flexible and systematically improvable framework for quantifying symmetry breaking in QCD. Applied to finite-temperature QCD, it leads to several central conclusions:

1. **RG-invariant diagnostics:** The κ_{AB} ratios furnish renormalization-group invariant, scheme-independent measures of symmetry breaking across different operator channels, allowing direct comparison between lattice spacings and formulations.

2. **Continuum convergence:** Although finite- a effects produce channel-dependent hierarchies, all nonsinglet κ_{AB} values converge consistently in the continuum limit, indicating a common restoration scale for different manifestations of chiral and axial symmetry in the connected sector.

3. **Hierarchical restoration:** Both $SU(2)_L \times SU(2)_R$ and $U(1)_A$ exhibit a two-stage restoration pattern in the crossover regime: first in the nonsinglet sector around $T_c^{\text{ns}} \sim 156$ MeV, and only at significantly higher temperature in the singlet sector, where suppression of topological fluctuations becomes essential.

4. **Clean singlet probes:** Tensor singlet channels provide theoretically clean, RG-invariant observables for testing full effective restoration— κ_{TX}^s for $U(1)_A$ and mixed singlet ratios for chiral symmetry—complementing direct measurements of the topological susceptibility χ_t .

Natural extensions include simulations at lighter quark masses to probe scaling behavior more directly, applications to additional operator and flavor sectors, and systematic comparison with functional renormalization-group and effective-model studies. More broadly, the κ_{AB} program establishes a quantitative benchmark for assessing symmetry realization in QCD and clarifies the relation between lattice observables and continuum effective descriptions of the chiral transition.

Combined with future continuum-extrapolated determinations of tensor singlet channels and overlap-fermion-based measurements of χ_t , this framework offers a comprehensive strategy for mapping the complete restoration pattern of chiral and axial symmetries in QCD.

A Meson Operator Notation

Table 5: Summary of meson operators and their corresponding regularized susceptibilities in $N_f = 2$ QCD. The notation follows eqs. (2.7)–(2.15) in the main text. Singlet (s) and nonsinglet (ns) channels are distinguished, with the latter involving only connected diagrams. Tensor operators T_k and X_k ($k = 1, 2, 3$) are defined with spatial index k .

Meson	Operator	Channel	Flavor	Susceptibility
π^a	$\bar{q}\gamma_5 t^a q$	Pseudoscalar (P)	Nonsinglet (ns)	$\chi_\pi = \chi_P^{ns}$
δ^a	$\bar{q}t^a q$	Scalar (S)	Nonsinglet (ns)	$\chi_\delta = \chi_S^{ns}$
σ	$\bar{q}q$	Scalar (S)	Singlet (s)	$\chi_\sigma = \chi_S^s$
η ($N_f = 2$)	$\bar{q}\gamma_5 q$	Pseudoscalar (P)	Singlet (s)	$\chi_\eta = \chi_P^s$
ρ^a	$\bar{q}\gamma_i t^a q$	Vector (V_i)	Nonsinglet (ns)	$\chi_\rho = \chi_{V_i}^{ns}$
a_1^a	$\bar{q}\gamma_5 \gamma_i t^a q$	Axial-vector (A_i)	Nonsinglet (ns)	$\chi_{a_1} = \chi_{A_i}^{ns}$
ω	$\bar{q}\gamma_i q$	Vector (V_i)	Singlet (s)	$\chi_\omega = \chi_{V_i}^s$
h_1	$\bar{q}\gamma_5 \gamma_i q$	Axial-vector (A_i)	Singlet (s)	$\chi_{h_1} = \chi_{A_i}^s$
ρ_T^a	$\bar{q}\gamma_4 \gamma_i t^a q$	Tensor (T_i)	Nonsinglet (ns)	$\chi_{\rho_T} = \chi_{T_i}^{ns}$
b_1^a	$\bar{q}\gamma_5 \gamma_4 \gamma_i t^a q$	Axial-tensor (X_i)	Nonsinglet (ns)	$\chi_{b_1} = \chi_{X_i}^{ns}$
ω_T	$\bar{q}\gamma_4 \gamma_i q$	Tensor (T_i)	Singlet (s)	$\chi_{\omega_T} = \chi_{T_i}^s$
h_{1T}	$\bar{q}\gamma_5 \gamma_4 \gamma_i q$	Axial-tensor (X_i)	Singlet (s)	$\chi_{h_{1T}} = \chi_{X_i}^s$

- For $N_f = 2$ flavor, the generators are $t^0 = \mathbf{1}/2$ (for flavor singlet) and $t^a = \tau^a/2$ ($a = 1, 2, 3$ for flavor nonsinglets), where $\mathbf{1}$ is the 2×2 identity matrix and τ^a are the Pauli matrices. They satisfy the normalization condition $\text{tr}(t^a t^b) = \delta^{ab}/2$ for all $a, b = 0, 1, 2, 3$.
- The flavor-singlet generator t^0 is always suppressed in our notation for singlet operators; e.g., we write $\bar{q}q$ to mean $\bar{q}t^0 q$, and similarly $\bar{q}\gamma_5 q$ for $\bar{q}\gamma_5 t^0 q$.
- Spatial index $i = 1, 2, 3$ (or $k = 1, 2, 3$) is implicit for vector and tensor channels.
- Singlet operators ($\sigma, \eta, \omega, h_1, \omega_T, h_{1T}$) involve disconnected diagrams and require careful subtraction of power divergences.
- Nonsinglet operators involve only connected diagrams and have cleaner renormalization properties.
- The tensor representations ρ_T^a (via T_i) and b_1^a (via X_i) probe $U(1)_A$ through a different Dirac structure than the scalar–pseudoscalar pair (δ – π).
- The vector singlet ω and axial-vector singlet h_1 are the $I = 0$ partners under $U(1)_A$, while the tensor singlet ω_T and axial-tensor singlet h_{1T} play analogous roles in the tensor channel.

B Tables of results

In this appendix, we provide numerical data of the figures in the main text. Specifically, the data for the time-correlation functions, regularized susceptibilities, and RG-invariant symmetry ratios for u, d off-diagonal flavor-nonsinglet mesons are presented in tabular form, corresponding to figures 1, 2, and 3, respectively.

The numerical values for the time-correlation functions $C_\Gamma(t)$ of the $\bar{u}\Gamma d$ on the $32^3 \times 16$ lattice, shown in figure 1, are tabulated in tables 6–8 for the (P, S, V, A, T, X) channels, for three lattice spacings $a = (0.075, 0.069, 0.064)$ fm.

Numerical results for the regularized susceptibilities $(\chi_S, \chi_P, \chi_V, \chi_A, \chi_T, \chi_X)$, presented in figure 2, are listed in tables 9–11. These tables also include the corresponding RG-invariant symmetry ratios κ_{PS} , κ_{VA} , and κ_{TX} , shown in figures 3. Data are provided for the same three lattice spacings across twelve temperatures ranging from 164 to 385 MeV.

Statistical uncertainties are estimated using the jackknife method with a bin size of 10–15 configurations of which the statistical error saturates. The numerical values are quoted with more significant figures than strictly warranted by the precision. This choice is intentional, to clearly resolve subtle differences—particularly between symmetry partners such as χ_V and χ_A —that might otherwise be obscured within the quoted error bars.

t/a	$C_P(t)$	$C_S(t)$	$C_V(t)$	$C_A(t)$	$C_T(t)$	$C_X(t)$
1	$3.926(15) \times 10^{-2}$	$3.919(15) \times 10^{-2}$	$2.9286(88) \times 10^{-2}$	$2.9285(88) \times 10^{-2}$	$2.1937(41) \times 10^{-2}$	$2.1937(41) \times 10^{-2}$
2	$6.462(91) \times 10^{-3}$	$6.397(93) \times 10^{-3}$	$3.291(23) \times 10^{-3}$	$3.291(23) \times 10^{-3}$	$1.971(14) \times 10^{-3}$	$1.971(14) \times 10^{-3}$
3	$2.611(85) \times 10^{-3}$	$2.551(84) \times 10^{-3}$	$8.317(75) \times 10^{-4}$	$8.314(75) \times 10^{-4}$	$4.387(50) \times 10^{-4}$	$4.387(50) \times 10^{-4}$
4	$1.620(84) \times 10^{-3}$	$1.563(83) \times 10^{-3}$	$3.299(35) \times 10^{-4}$	$3.297(35) \times 10^{-4}$	$1.682(26) \times 10^{-4}$	$1.682(26) \times 10^{-4}$
5	$1.238(83) \times 10^{-3}$	$1.184(82) \times 10^{-3}$	$1.754(23) \times 10^{-4}$	$1.752(23) \times 10^{-4}$	$9.16(19) \times 10^{-5}$	$9.16(19) \times 10^{-5}$
6	$1.062(82) \times 10^{-3}$	$1.012(81) \times 10^{-3}$	$1.160(17) \times 10^{-4}$	$1.159(17) \times 10^{-4}$	$6.35(16) \times 10^{-5}$	$6.35(16) \times 10^{-5}$
7	$9.82(81) \times 10^{-4}$	$9.34(81) \times 10^{-4}$	$9.19(16) \times 10^{-5}$	$9.18(16) \times 10^{-5}$	$5.24(14) \times 10^{-5}$	$5.25(15) \times 10^{-5}$
8	$9.61(80) \times 10^{-4}$	$9.13(81) \times 10^{-4}$	$8.52(16) \times 10^{-5}$	$8.51(16) \times 10^{-5}$	$4.92(14) \times 10^{-5}$	$4.93(14) \times 10^{-5}$
9	$9.90(79) \times 10^{-4}$	$9.41(80) \times 10^{-4}$	$9.24(17) \times 10^{-5}$	$9.23(17) \times 10^{-5}$	$5.23(17) \times 10^{-5}$	$5.24(18) \times 10^{-5}$
1	$1.077(77) \times 10^{-3}$	$1.026(79) \times 10^{-3}$	$1.176(18) \times 10^{-4}$	$1.175(18) \times 10^{-4}$	$6.35(19) \times 10^{-5}$	$6.35(19) \times 10^{-5}$
11	$1.259(75) \times 10^{-3}$	$1.204(78) \times 10^{-3}$	$1.775(21) \times 10^{-4}$	$1.774(21) \times 10^{-4}$	$9.14(19) \times 10^{-5}$	$9.13(19) \times 10^{-5}$
12	$1.645(72) \times 10^{-3}$	$1.585(75) \times 10^{-3}$	$3.326(32) \times 10^{-4}$	$3.324(32) \times 10^{-4}$	$1.681(25) \times 10^{-4}$	$1.681(25) \times 10^{-4}$
13	$2.645(71) \times 10^{-3}$	$2.579(75) \times 10^{-3}$	$8.384(53) \times 10^{-4}$	$8.381(53) \times 10^{-4}$	$4.425(42) \times 10^{-4}$	$4.424(42) \times 10^{-4}$
14	$6.521(74) \times 10^{-3}$	$6.450(80) \times 10^{-3}$	$3.322(17) \times 10^{-3}$	$3.322(17) \times 10^{-3}$	$1.996(10) \times 10^{-3}$	$1.996(11) \times 10^{-3}$
15	$3.940(12) \times 10^{-2}$	$3.933(11) \times 10^{-2}$	$2.9396(71) \times 10^{-2}$	$2.9395(71) \times 10^{-2}$	$2.2020(44) \times 10^{-2}$	$2.2019(44) \times 10^{-2}$

Table 6: Time-correlation function $C_\Gamma(t)$ of $\bar{u}\Gamma d$ for P, S, V, A, T, X channels on the $32^3 \times 16$ lattice with lattice spacing $a=0.075$ fm.

t/a	$C_P(t)$	$C_S(t)$	$C_V(t)$	$C_A(t)$	$C_T(t)$	$C_X(t)$
1	$3.944(11) \times 10^{-2}$	$3.943(11) \times 10^{-2}$	$2.9601(71) \times 10^{-2}$	$2.9601(71) \times 10^{-2}$	$2.2085(44) \times 10^{-2}$	$2.2085(44) \times 10^{-2}$
2	$6.304(64) \times 10^{-3}$	$6.295(63) \times 10^{-3}$	$3.377(15) \times 10^{-3}$	$3.376(15) \times 10^{-3}$	$2.0059(93) \times 10^{-3}$	$2.0057(93) \times 10^{-3}$
3	$2.368(59) \times 10^{-3}$	$2.360(58) \times 10^{-3}$	$8.639(57) \times 10^{-4}$	$8.638(57) \times 10^{-4}$	$4.479(37) \times 10^{-4}$	$4.478(37) \times 10^{-4}$
4	$1.349(55) \times 10^{-3}$	$1.342(54) \times 10^{-3}$	$3.463(26) \times 10^{-4}$	$3.462(26) \times 10^{-4}$	$1.719(19) \times 10^{-4}$	$1.718(19) \times 10^{-4}$
5	$9.60(52) \times 10^{-4}$	$9.54(51) \times 10^{-4}$	$1.850(16) \times 10^{-4}$	$1.849(16) \times 10^{-4}$	$9.28(14) \times 10^{-5}$	$9.27(14) \times 10^{-5}$
6	$7.83(50) \times 10^{-4}$	$7.77(49) \times 10^{-4}$	$1.222(13) \times 10^{-4}$	$1.221(13) \times 10^{-4}$	$6.34(12) \times 10^{-5}$	$6.33(12) \times 10^{-5}$
7	$7.01(50) \times 10^{-4}$	$6.95(49) \times 10^{-4}$	$9.63(12) \times 10^{-5}$	$9.62(12) \times 10^{-5}$	$5.14(16) \times 10^{-5}$	$5.14(16) \times 10^{-5}$
8	$6.77(50) \times 10^{-4}$	$6.70(49) \times 10^{-4}$	$8.93(15) \times 10^{-5}$	$8.92(15) \times 10^{-5}$	$4.81(16) \times 10^{-5}$	$4.80(16) \times 10^{-5}$
9	$7.02(51) \times 10^{-4}$	$6.95(50) \times 10^{-4}$	$9.71(19) \times 10^{-5}$	$9.70(19) \times 10^{-5}$	$5.16(17) \times 10^{-5}$	$5.15(17) \times 10^{-5}$
10	$7.87(52) \times 10^{-4}$	$7.79(51) \times 10^{-4}$	$1.239(23) \times 10^{-4}$	$1.239(23) \times 10^{-4}$	$6.40(17) \times 10^{-5}$	$6.39(17) \times 10^{-5}$
11	$9.71(54) \times 10^{-4}$	$9.61(53) \times 10^{-4}$	$1.877(31) \times 10^{-4}$	$1.876(31) \times 10^{-4}$	$9.43(14) \times 10^{-5}$	$9.42(14) \times 10^{-5}$
12	$1.363(58) \times 10^{-3}$	$1.352(57) \times 10^{-3}$	$3.489(41) \times 10^{-4}$	$3.488(41) \times 10^{-4}$	$1.738(22) \times 10^{-4}$	$1.738(22) \times 10^{-4}$
13	$2.377(65) \times 10^{-3}$	$2.365(63) \times 10^{-3}$	$8.631(68) \times 10^{-4}$	$8.630(68) \times 10^{-4}$	$4.495(40) \times 10^{-4}$	$4.494(40) \times 10^{-4}$
14	$6.28(11) \times 10^{-3}$	$6.26(10) \times 10^{-3}$	$3.356(19) \times 10^{-3}$	$3.356(19) \times 10^{-3}$	$1.998(11) \times 10^{-3}$	$1.998(11) \times 10^{-3}$
15	$3.927(11) \times 10^{-2}$	$3.926(11) \times 10^{-2}$	$2.9478(74) \times 10^{-2}$	$2.9478(74) \times 10^{-2}$	$2.2017(45) \times 10^{-2}$	$2.2017(45) \times 10^{-2}$

Table 7: Time-correlation function $C_\Gamma(t)$ of $\bar{u}\Gamma d$ for P, S, V, A, T, X channels on the $32^3 \times 16$ lattice with lattice spacing $a=0.069$ fm.

t/a	$C_P(t)$	$C_S(t)$	$C_V(t)$	$C_A(t)$	$C_T(t)$	$C_X(t)$
1	$3.9219(97) \times 10^{-2}$	$3.9215(97) \times 10^{-2}$	$2.9480(64) \times 10^{-2}$	$2.9480(64) \times 10^{-2}$	$2.1966(39) \times 10^{-2}$	$2.1966(39) \times 10^{-2}$
2	$6.238(31) \times 10^{-3}$	$6.234(31) \times 10^{-3}$	$3.389(15) \times 10^{-3}$	$3.389(15) \times 10^{-3}$	$2.0051(86) \times 10^{-3}$	$2.0051(86) \times 10^{-3}$
3	$2.307(32) \times 10^{-3}$	$2.304(32) \times 10^{-3}$	$8.733(45) \times 10^{-4}$	$8.732(45) \times 10^{-4}$	$4.506(28) \times 10^{-4}$	$4.506(28) \times 10^{-4}$
4	$1.287(27) \times 10^{-3}$	$1.284(27) \times 10^{-3}$	$3.508(21) \times 10^{-4}$	$3.508(21) \times 10^{-4}$	$1.735(16) \times 10^{-4}$	$1.735(16) \times 10^{-4}$
5	$8.96(26) \times 10^{-4}$	$8.93(25) \times 10^{-4}$	$1.861(13) \times 10^{-4}$	$1.861(13) \times 10^{-4}$	$9.34(17) \times 10^{-5}$	$9.34(17) \times 10^{-5}$
6	$7.17(25) \times 10^{-4}$	$7.14(25) \times 10^{-4}$	$1.210(11) \times 10^{-4}$	$1.210(11) \times 10^{-4}$	$6.34(17) \times 10^{-5}$	$6.34(17) \times 10^{-5}$
7	$6.37(25) \times 10^{-4}$	$6.34(25) \times 10^{-4}$	$9.36(12) \times 10^{-5}$	$9.36(12) \times 10^{-5}$	$5.11(16) \times 10^{-5}$	$5.10(16) \times 10^{-5}$
8	$6.16(26) \times 10^{-4}$	$6.13(26) \times 10^{-4}$	$8.56(12) \times 10^{-5}$	$8.55(12) \times 10^{-5}$	$4.74(21) \times 10^{-5}$	$4.74(21) \times 10^{-5}$
9	$6.45(27) \times 10^{-4}$	$6.42(27) \times 10^{-4}$	$9.24(16) \times 10^{-5}$	$9.24(16) \times 10^{-5}$	$5.04(21) \times 10^{-5}$	$5.04(21) \times 10^{-5}$
10	$7.32(28) \times 10^{-4}$	$7.29(28) \times 10^{-4}$	$1.186(16) \times 10^{-4}$	$1.186(17) \times 10^{-4}$	$6.22(22) \times 10^{-5}$	$6.22(22) \times 10^{-5}$
11	$9.15(29) \times 10^{-4}$	$9.12(28) \times 10^{-4}$	$1.825(19) \times 10^{-4}$	$1.825(19) \times 10^{-4}$	$9.19(25) \times 10^{-5}$	$9.19(25) \times 10^{-5}$
12	$1.307(29) \times 10^{-3}$	$1.304(29) \times 10^{-3}$	$3.465(22) \times 10^{-4}$	$3.465(22) \times 10^{-4}$	$1.720(24) \times 10^{-4}$	$1.720(24) \times 10^{-4}$
13	$2.323(30) \times 10^{-3}$	$2.319(29) \times 10^{-3}$	$8.692(46) \times 10^{-4}$	$8.692(46) \times 10^{-4}$	$4.508(35) \times 10^{-4}$	$4.507(35) \times 10^{-4}$
14	$6.256(29) \times 10^{-3}$	$6.253(29) \times 10^{-3}$	$3.396(13) \times 10^{-3}$	$3.395(13) \times 10^{-3}$	$2.0141(80) \times 10^{-3}$	$2.0141(80) \times 10^{-3}$
15	$3.9292(82) \times 10^{-2}$	$3.9288(82) \times 10^{-2}$	$2.9539(54) \times 10^{-2}$	$2.9538(54) \times 10^{-2}$	$2.2012(33) \times 10^{-2}$	$2.2012(33) \times 10^{-2}$

Table 8: Time-correlation function $C_\Gamma(t)$ of $\bar{u}\Gamma d$ for P, S, V, A, T, X channels on the $32^3 \times 16$ lattice with lattice spacing $a=0.064$ fm.

T [MeV]	a [fm]	χ_S	χ_P	κ_{PS}
164	0.075	$5.34324e-2 \pm 6.014e-4$	$5.38707e-2 \pm 5.882e-4$	$4.0846e-3 \pm 1.0146e-3$
179	0.069	$5.20737e-2 \pm 3.699e-4$	$5.21386e-2 \pm 3.797e-4$	$6.2278e-4 \pm 2.9024e-4$
192	0.064	$5.15927e-2 \pm 1.981e-4$	$5.16162e-2 \pm 1.985e-4$	$2.2824e-4 \pm 6.641e-5$
219	0.075	$5.02095e-2 \pm 1.606e-4$	$5.02886e-2 \pm 1.566e-4$	$7.8791e-4 \pm 1.8618e-4$
238	0.069	$5.01252e-2 \pm 2.235e-4$	$5.01403e-2 \pm 2.260e-4$	$1.5054e-4 \pm 3.545e-5$
257	0.064	$4.96265e-2 \pm 1.391e-4$	$4.96309e-2 \pm 1.389e-4$	$4.4259e-5 \pm 2.0238e-5$
263	0.075	$4.79896e-2 \pm 1.793e-4$	$4.80188e-2 \pm 1.790e-4$	$3.0421e-4 \pm 5.490e-5$
286	0.069	$4.80414e-2 \pm 1.190e-4$	$4.80473e-2 \pm 1.193e-4$	$6.1439e-5 \pm 1.1913e-5$
308	0.064	$4.81840e-2 \pm 1.089e-4$	$4.81862e-2 \pm 1.089e-4$	$2.3046e-5 \pm 5.357e-6$
328	0.075	$4.69035e-2 \pm 1.273e-4$	$4.69140e-2 \pm 1.259e-4$	$1.1254e-4 \pm 4.477e-5$
357	0.069	$4.68727e-2 \pm 1.649e-4$	$4.68751e-2 \pm 1.657e-4$	$2.5877e-5 \pm 6.983e-6$
385	0.064	$4.69490e-2 \pm 1.166e-4$	$4.69499e-2 \pm 1.166e-4$	$9.5128e-6 \pm 3.3590e-6$

Table 9: Scalar and pseudoscalar susceptibilities χ_S , χ_P and the RG-invariant symmetry ratio κ_{PS} for three lattice spacings and twelve temperatures.

T [MeV]	a [fm]	χ_V	χ_A	κ_{VA}
164	0.075	$3.416665e-2 \pm 8.403e-5$	$3.416499e-2 \pm 8.402e-5$	$2.4248e-5 \pm 2.080e-6$
179	0.069	$3.456805e-2 \pm 7.824e-5$	$3.456716e-2 \pm 7.824e-5$	$1.2819e-5 \pm 1.806e-6$
192	0.064	$3.456541e-2 \pm 6.396e-5$	$3.456498e-2 \pm 6.395e-5$	$6.2764e-6 \pm 4.664e-7$
219	0.075	$3.414924e-2 \pm 9.063e-5$	$3.414868e-2 \pm 9.063e-5$	$8.1562e-6 \pm 9.217e-7$
238	0.069	$3.448263e-2 \pm 6.622e-5$	$3.448232e-2 \pm 6.622e-5$	$4.5307e-6 \pm 2.865e-7$
257	0.064	$3.460791e-2 \pm 6.813e-5$	$3.460776e-2 \pm 6.813e-5$	$2.2422e-6 \pm 3.596e-7$
263	0.075	$3.412941e-2 \pm 8.999e-5$	$3.412913e-2 \pm 8.999e-5$	$4.0453e-6 \pm 3.488e-7$
286	0.069	$3.446740e-2 \pm 5.640e-5$	$3.446724e-2 \pm 5.640e-5$	$2.2984e-6 \pm 8.424e-8$
308	0.064	$3.472431e-2 \pm 7.547e-5$	$3.472421e-2 \pm 7.547e-5$	$1.4126e-6 \pm 5.159e-8$
328	0.075	$3.384798e-2 \pm 7.409e-5$	$3.384784e-2 \pm 7.409e-5$	$2.1217e-6 \pm 2.826e-7$
357	0.069	$3.449452e-2 \pm 8.048e-5$	$3.449444e-2 \pm 8.048e-5$	$1.2518e-6 \pm 1.138e-7$
385	0.064	$3.478435e-2 \pm 7.885e-5$	$3.478430e-2 \pm 7.885e-5$	$6.8488e-7 \pm 1.704e-8$

Table 10: Vector and axial-vector susceptibilities χ_V , χ_A and the RG-invariant symmetry ratio κ_{VA} for three lattice spacings and twelve temperatures.

T [MeV]	a [fm]	χ_T	χ_X	κ_{TX}
164	0.075	$2.480619\text{e-}2 \pm 6.076\text{e-}5$	$2.480472\text{e-}2 \pm 6.071\text{e-}5$	$2.9511\text{e-}5 \pm 1.3839\text{e-}5$
179	0.069	$2.489018\text{e-}2 \pm 4.489\text{e-}5$	$2.488948\text{e-}2 \pm 4.490\text{e-}5$	$1.3890\text{e-}5 \pm 3.475\text{e-}6$
192	0.064	$2.487534\text{e-}2 \pm 3.871\text{e-}5$	$2.487512\text{e-}2 \pm 3.871\text{e-}5$	$4.4736\text{e-}6 \pm 5.302\text{e-}7$
219	0.075	$2.490372\text{e-}2 \pm 5.385\text{e-}5$	$2.490318\text{e-}2 \pm 5.379\text{e-}5$	$1.0886\text{e-}5 \pm 3.168\text{e-}6$
238	0.069	$2.498616\text{e-}2 \pm 4.239\text{e-}5$	$2.498592\text{e-}2 \pm 4.239\text{e-}5$	$4.9238\text{e-}6 \pm 3.050\text{e-}7$
257	0.064	$2.508379\text{e-}2 \pm 3.896\text{e-}5$	$2.508370\text{e-}2 \pm 3.896\text{e-}5$	$1.9293\text{e-}6 \pm 1.303\text{e-}7$
263	0.075	$2.516102\text{e-}2 \pm 4.261\text{e-}5$	$2.516079\text{e-}2 \pm 4.261\text{e-}5$	$4.4966\text{e-}6 \pm 9.353\text{e-}7$
286	0.069	$2.526107\text{e-}2 \pm 3.355\text{e-}5$	$2.526093\text{e-}2 \pm 3.355\text{e-}5$	$2.7641\text{e-}6 \pm 2.086\text{e-}7$
308	0.064	$2.536585\text{e-}2 \pm 4.611\text{e-}5$	$2.536578\text{e-}2 \pm 4.611\text{e-}5$	$1.2422\text{e-}6 \pm 1.613\text{e-}7$
328	0.075	$2.537214\text{e-}2 \pm 4.411\text{e-}5$	$2.537201\text{e-}2 \pm 4.411\text{e-}5$	$2.4743\text{e-}6 \pm 6.449\text{e-}7$
357	0.069	$2.561389\text{e-}2 \pm 5.092\text{e-}5$	$2.561378\text{e-}2 \pm 5.092\text{e-}5$	$2.0030\text{e-}6 \pm 4.424\text{e-}7$
385	0.064	$2.578521\text{e-}2 \pm 4.603\text{e-}5$	$2.578517\text{e-}2 \pm 4.603\text{e-}5$	$7.8727\text{e-}7 \pm 2.746\text{e-}8$

Table 11: Tensor-vector and axial-tensor-vector susceptibilities χ_T , χ_X and the RG-invariant symmetry ratio κ_{TX} for three lattice spacings and twelve temperatures.

Acknowledgments

We are grateful to Academia Sinica Grid Computing Center and National Center for High Performance Computing for the computer time and facilities. This work was supported by the National Science and Technology Council (Grants No. 108-2112-M-003-005, No. 109-2112-M-003-006, No. 110-2112-M-003-009), and Academia Sinica Grid Computing Centre (Grant No. AS-CFII-112-103).

References

- [1] Y. Nambu and G. Jona-Lasinio, “Dynamical model of elementary particles based on an analogy with Superconductivity. I.”, *Phys. Rev.* **122**, 345-358 (1961)
- [2] Y. Nambu and G. Jona-Lasinio, “Dynamical model of elementary particles based on an analogy with superconductivity. II.”, *Phys. Rev.* **124**, 246-254 (1961)
- [3] S. L. Adler, “Axial vector vertex in spinor electrodynamics”, *Phys. Rev.* **177**, 2426-2438 (1969)
- [4] J. S. Bell and R. Jackiw, “A PCAC puzzle: $\pi^0 \rightarrow \gamma\gamma$ in the σ model”, *Nuovo Cim. A* **60**, 47-61 (1969)
- [5] K. Fujikawa, “Path Integral Measure for Gauge Invariant Fermion Theories”, *Phys. Rev. Lett.* **42**, 1195-1198 (1979)
- [6] G. 't Hooft, “Computation of the Quantum Effects Due to a Four-Dimensional Pseudoparticle”, *Phys. Rev. D* **14**, 3432-3450 (1976) [erratum: *Phys. Rev. D* **18**, 2199 (1978)]
- [7] E. Witten, “Current Algebra Theorems for the U(1) Goldstone Boson”, *Nucl. Phys. B* **156**, 269-283 (1979)
- [8] G. Veneziano, “U(1) Without Instantons”, *Nucl. Phys. B* **159**, 213-224 (1979)
- [9] Y. Aoki, G. Endrodi, Z. Fodor, S. D. Katz and K. K. Szabo, “The Order of the quantum chromodynamics transition predicted by the standard model of particle physics”, *Nature* **443**, 675-678 (2006) [arXiv:hep-lat/0611014 [hep-lat]].
- [10] S. Borsanyi, Z. Fodor, C. Hoelbling, S. D. Katz, S. Krieg and K. K. Szabo, “Full result for the QCD equation of state with 2+1 flavors”, *Phys. Lett. B* **730**, 99-104 (2014) [arXiv:1309.5258 [hep-lat]].
- [11] A. Bazavov *et al.* [HotQCD], “Equation of state in (2+1)-flavor QCD”, *Phys. Rev. D* **90**, 094503 (2014) [arXiv:1407.6387 [hep-lat]].
- [12] A. Bazavov *et al.* [HotQCD], “Chiral crossover in QCD at zero and non-zero chemical potentials”, *Phys. Lett. B* **795**, 15-21 (2019) [arXiv:1812.08235 [hep-lat]].
- [13] S. Borsanyi, Z. Fodor, J. N. Guenther, R. Kara, S. D. Katz, P. Parotto, A. Pasztor, C. Ratti and K. K. Szabo, “QCD Crossover at Finite Chemical Potential from Lattice Simulations”, *Phys. Rev. Lett.* **125**, no.5, 052001 (2020) [arXiv:2002.02821 [hep-lat]].
- [14] R. D. Pisarski and F. Wilczek, “Remarks on the Chiral Phase Transition in Chromodynamics”, *Phys. Rev. D* **29**, 338-341 (1984)
- [15] H. Leutwyler and A. V. Smilga, “Spectrum of Dirac operator and role of winding number in QCD”, *Phys. Rev. D* **46**, 5607-5632 (1992)

- [16] T. D. Cohen, “QCD inequalities, the high temperature phase of QCD, and $U(1)_A$ symmetry”, *Phys. Rev. D* **54**, R1867-R1870 (1996) [arXiv:hep-ph/9601216 [hep-ph]].
- [17] S. Aoki, H. Fukaya and Y. Taniguchi, “Chiral symmetry restoration, eigenvalue density of Dirac operator and axial $U(1)$ anomaly at finite temperature”, *Phys. Rev. D* **86**, 114512 (2012) [arXiv:1209.2061 [hep-lat]].
- [18] G. Cossu, S. Aoki, H. Fukaya, S. Hashimoto, T. Kaneko, H. Matsufuru and J. I. Noaki, “Finite temperature study of the axial $U(1)$ symmetry on the lattice with overlap fermion formulation,” *Phys. Rev. D* **87**, no.11, 114514 (2013) [erratum: *Phys. Rev. D* **88**, no.1, 019901 (2013)] [arXiv:1304.6145 [hep-lat]].
- [19] M. I. Buchoff, M. Cheng, N. H. Christ, H. T. Ding, C. Jung, F. Karsch, Z. Lin, R. D. Mawhinney, S. Mukherjee and P. Petreczky, *et al.* “QCD chiral transition, $U(1)_A$ symmetry and the Dirac spectrum using domain wall fermions”, *Phys. Rev. D* **89**, no.5, 054514 (2014) [arXiv:1309.4149 [hep-lat]].
- [20] B. B. Brandt, A. Francis, H. B. Meyer, O. Philipsen, D. Robaina and H. Wittig, “On the strength of the $U_A(1)$ anomaly at the chiral phase transition in $N_f = 2$ QCD”, *JHEP* **12**, 158 (2016) [arXiv:1608.06882 [hep-lat]].
- [21] A. Tomiya, G. Cossu, S. Aoki, H. Fukaya, S. Hashimoto, T. Kaneko and J. Noaki, “Evidence of effective axial $U(1)$ symmetry restoration at high temperature QCD”, *Phys. Rev. D* **96**, no.3, 034509 (2017); **96**, A079902 (2017). [arXiv:1612.01908 [hep-lat]].
- [22] H. T. Ding, S. T. Li, S. Mukherjee, A. Tomiya, X. D. Wang and Y. Zhang, “Correlated Dirac Eigenvalues and Axial Anomaly in Chiral Symmetric QCD”, *Phys. Rev. Lett.* **126**, no.8, 082001 (2021) [arXiv:2010.14836 [hep-lat]].
- [23] O. Kaczmarek, R. Shanker and S. Sharma, “Eigenvalues of the QCD Dirac matrix with improved staggered quarks in the continuum limit”, *Phys. Rev. D* **108**, no.9, 094501 (2023) [arXiv:2301.11610 [hep-lat]].
- [24] S. Aoki *et al.* [JLQCD], “Study of the axial $U(1)$ anomaly at high temperature with lattice chiral fermions”, *Phys. Rev. D* **103**, no.7, 074506 (2021) [arXiv:2011.01499 [hep-lat]].
- [25] T. W. Chiu, “Symmetries of meson correlators in high-temperature QCD with physical (u/d,s,c) domain-wall quarks”, *Phys. Rev. D* **107**, no.11, 114501 (2023) [arXiv:2302.06073 [hep-lat]].
- [26] R. V. Gavai, M. E. Jaensch, O. Kaczmarek, F. Karsch, M. Sarkar, R. Shanker, S. Sharma, S. Sharma and T. Ueding, “Aspects of the chiral crossover transition in (2+1)-flavor QCD with Möbius domain-wall fermions”, *Phys. Rev. D* **111**, no.3, 034507 (2025) [arXiv:2411.10217 [hep-lat]].
- [27] D. B. Kaplan, “A Method for simulating chiral fermions on the lattice”, *Phys. Lett. B* **288**, 342-347 (1992) [arXiv:hep-lat/9206013 [hep-lat]].
- [28] D. B. Kaplan, “Chiral fermions on the lattice”, *Nucl. Phys. B Proc. Suppl.* **30**, 597-600 (1993)
- [29] H. Neuberger, “Exactly massless quarks on the lattice”, *Phys. Lett. B* **417**, 141-144 (1998) [arXiv:hep-lat/9707022 [hep-lat]].
- [30] R. Narayanan and H. Neuberger, “A Construction of lattice chiral gauge theories”, *Nucl. Phys. B* **443**, 305-385 (1995) [arXiv:hep-th/9411108 [hep-th]].
- [31] T. W. Chiu, “Symmetries of spatial correlators of light and heavy mesons in high temperature lattice QCD”, *Phys. Rev. D* **110**, no.1, 014502 (2024) [arXiv:2404.15932 [hep-lat]].

- [32] T. W. Chiu, “Symmetries in High-Temperature Lattice QCD with (u, d, s, c, b) Optimal Domain-Wall Quarks”, *Symmetry* **17**, no.5, 700 (2025) [arXiv:2411.16705 [hep-lat]].
- [33] G. Martinelli, C. Pittori, C. T. Sachrajda, M. Testa and A. Vladikas, “A general method for nonperturbative renormalization of lattice operators”, *Nucl. Phys. B* **445**, 81-108 (1995) [arXiv:hep-lat/9411010 [hep-lat]].
- [34] T. W. Chiu, “Optimal lattice domain wall fermions”, *Phys. Rev. Lett.* **90**, 071601 (2003) [hep-lat/0209153];
- [35] T. W. Chiu, “Domain-Wall Fermion with R_5 Symmetry”, *Phys. Lett. B* **744**, 95 (2015) [arXiv:1503.01750 [hep-lat]].
- [36] K. G. Wilson, “Confinement of Quarks”, *Phys. Rev. D* **10**, 2445-2459 (1974)
- [37] T. W. Chiu, T. H. Hsieh, Y. Y. Mao [TWQCD Collaboration], “Pseudoscalar Meson in Two Flavors QCD with the Optimal Domain-Wall Fermion”, *Phys. Lett. B* **717**, 420 (2012) [arXiv:1109.3675 [hep-lat]].
- [38] Y. C. Chen, T. W. Chiu [TWQCD Collaboration], “Exact Pseudofermion Action for Monte Carlo Simulation of Domain-Wall Fermion”, *Phys. Lett. B* **738**, 55 (2014) [arXiv:1403.1683 [hep-lat]].
- [39] Y. C. Chen, T. W. Chiu and T. H. Hsieh [TWQCD Collaboration], “Topological susceptibility in finite temperature QCD with physical (u/d,s,c) domain-wall quarks”, *Phys. Rev. D* **106**, no.7, 074501 (2022) [arXiv:2204.01556 [hep-lat]].
- [40] R. Narayanan and H. Neuberger, “Infinite N phase transitions in continuum Wilson loop operators”, *JHEP* **0603**, 064 (2006) [hep-th/0601210].
- [41] M. Luscher, “Properties and uses of the Wilson flow in lattice QCD”, *JHEP* **1008**, 071 (2010); Erratum: [*JHEP* **1403**, 092 (2014)] [arXiv:1006.4518 [hep-lat]].
- [42] A. Bazavov *et al.* [MILC Collaboration], “Gradient flow and scale setting on MILC HISQ ensembles”, *Phys. Rev. D* **93**, no. 9, 094510 (2016) [arXiv:1503.02769 [hep-lat]].
- [43] Y. C. Chen, T. W. Chiu [TWQCD Collaboration], “Chiral Symmetry and the Residual Mass in Lattice QCD with the Optimal Domain-Wall Fermion”, *Phys. Rev. D* **86**, 094508 (2012) [arXiv:1205.6151 [hep-lat]].
- [44] T. W. Chiu, “Ginsparg-Wilson fermion propagators and chiral condensate”, *Phys. Rev. D* **60**, 034503 (1999) [arXiv:hep-lat/9810052 [hep-lat]].
- [45] P. Petreczky, H. P. Schadler and S. Sharma, “The topological susceptibility in finite temperature QCD and axion cosmology”, *Phys. Lett. B* **762**, 498-505 (2016) [arXiv:1606.03145 [hep-lat]].
- [46] S. Borsanyi, Z. Fodor, J. Guenther, K. H. Kampert, S. D. Katz, T. Kawanai, T. G. Kovacs, S. W. Mages, A. Pasztor and F. Pittler, *et al.* “Calculation of the axion mass based on high-temperature lattice quantum chromodynamics”, *Nature* **539**, no.7627, 69-71 (2016) [arXiv:1606.07494 [hep-lat]].
- [47] A. Athenodorou, C. Bonanno, C. Bonati, G. Clemente, F. D’Angelo, M. D’Elia, L. Maio, G. Martinelli, F. Sanfilippo and A. Todaro, “Topological susceptibility of $N_f = 2 + 1$ QCD from staggered fermions spectral projectors at high temperatures”, *JHEP* **10**, 197 (2022) [arXiv:2208.08921 [hep-lat]].

- [48] A. Y. Kotov, M. P. Lombardo and A. Trunin, “Topological observables and θ dependence in high temperature QCD from lattice simulations”, *JHEP* **09**, 045 (2025) [arXiv:2502.15407 [hep-lat]].
- [49] Y. Y. Mao and T. W. Chiu [TWQCD Collaboration], “Topological Susceptibility to the One-Loop Order in Chiral Perturbation Theory,” *Phys. Rev. D* **80**, 034502 (2009) [arXiv:0903.2146 [hep-lat]].
- [50] D. J. Gross, R. D. Pisarski and L. G. Yaffe, “QCD and Instantons at Finite Temperature”, *Rev. Mod. Phys.* **53**, 43 (1981)
- [51] L. Y. Glozman, “SU(4) symmetry of the dynamical QCD string and genesis of hadron spectra, *Eur. Phys. J. A* **51**, no.3, 27 (2015) [arXiv:1407.2798 [hep-ph]].
- [52] C. Rohrhofer, Y. Aoki, G. Cossu, H. Fukaya, C. Gattringer, L. Y. Glozman, S. Hashimoto, C. B. Lang and S. Prelovsek, “Symmetries of spatial meson correlators in high temperature QCD”, *Phys. Rev. D* **100**, no.1, 014502 (2019) [arXiv:1902.03191 [hep-lat]].
- [53] C. Rohrhofer, Y. Aoki, L. Y. Glozman and S. Hashimoto, “Chiral-spin symmetry of the meson spectral function above T_c ”, *Phys. Lett. B* **802**, 135245 (2020) [arXiv:1909.00927 [hep-lat]].
- [54] A. Alexandru and I. Horváth, “Possible New Phase of Thermal QCD,” *Phys. Rev. D* **100**, no.9, 094507 (2019) [arXiv:1906.08047 [hep-lat]].
- [55] X. L. Meng *et al.* [χ QCD and CLQCD], “Separation of infrared and bulk in thermal QCD”, *JHEP* **12**, 101 (2024) [arXiv:2305.09459 [hep-lat]].
- [56] G. 't Hooft, “On the Phase Transition Towards Permanent Quark Confinement,” *Nucl. Phys. B* **138**, 1-25 (1978)
- [57] J. A. Mickleley, C. Allton, R. Bignell and D. B. Leinweber, “Center vortex evidence for a second finite-temperature QCD transition”, *Phys. Rev. D* **111**, no.3, 034508 (2025) [arXiv:2411.19446 [hep-lat]].
- [58] A. Pelissetto and E. Vicari, “Relevance of the axial anomaly at the finite-temperature chiral transition in QCD”, *Phys. Rev. D* **88**, no.10, 105018 (2013) [arXiv:1309.5446 [hep-lat]].
- [59] J. P. Klinger, R. Kaiser and O. Philipsen, “The order of the chiral phase transition in massless many-flavour lattice QCD,” *PoS LATTICE2024*, 172 (2025) [arXiv:2501.19251 [hep-lat]].
- [60] A. Y. Kotov, M. P. Lombardo and A. Trunin, “QCD transition at the physical point, and its scaling window from twisted mass Wilson fermions,” *Phys. Lett. B* **823**, 136749 (2021) [arXiv:2105.09842 [hep-lat]].
- [61] J. Braun, W. j. Fu, J. M. Pawłowski, F. Rennecke, D. Rosenblüh and S. Yin, “Chiral susceptibility in (2+1)-flavor QCD”, *Phys. Rev. D* **102**, no.5, 056010 (2020) [arXiv:2003.13112 [hep-ph]].